

# A Survey of Small-Scale Waves and Wave-Like Phenomena in Jupiter's Atmosphere Detected by JunoCam

Glenn S. Orton<sup>1</sup>, Fachreddin Tabataba-Vakili<sup>1</sup>, Gerald Eichstädt<sup>2</sup>, John Rogers<sup>3</sup>,  
Candice J. Hansen<sup>4</sup>, Thomas W. Momary<sup>1</sup>, Andrew P. Ingersoll<sup>5</sup>, Shawn Brueshaber<sup>6</sup>, Michael  
H. Wong<sup>7</sup>, Amy A. Simon<sup>8</sup>, Leigh N. Fletcher<sup>9</sup>, Michael Ravine<sup>10</sup>, Michael Caplinger<sup>10</sup>, Dakota  
Smith<sup>11</sup>, Scott J. Bolton<sup>12</sup>, Stephen M. Levin<sup>1</sup>, James A. Sinclair<sup>1</sup>, Chloe Thepenier<sup>13</sup>, Hamish  
Nicholson<sup>14</sup>, Abigail Anthony<sup>15</sup>

<sup>1</sup>Jet Propulsion Laboratory, California Institute of Technology, Pasadena, California, USA

<sup>2</sup>Independent scholar, Stuttgart, Germany

<sup>3</sup>British Astronomical Association, London, UK

<sup>4</sup>Planetary Science Institute, Tucson, Arizona, USA

<sup>5</sup>California Institute of Technology, Pasadena, California, USA

<sup>6</sup>Western Michigan University, Kalamazoo, Michigan, USA

<sup>7</sup>University of California, Berkeley, California, USA; SETI Institute, Mountain View, California, USA

<sup>8</sup>NASA Goddard Space Flight Center, Greenbelt, Maryland, USA

<sup>9</sup>University of Leicester, Leicester, UK

<sup>10</sup>Malin Space Science Systems, San Diego, California, USA

<sup>11</sup>National Center for Atmospheric Research, Boulder, Colorado, USA

<sup>12</sup>Southwest Research Institute, San Antonio, Texas, USA

<sup>13</sup>Glendale Community College, Glendale, California, USA†

<sup>14</sup>Harvard College, Cambridge, Massachusetts, USA

<sup>15</sup>Golden West College, Huntington Beach, California, USA††

Corresponding author: Glenn Orton (glenn.orton@jpl.nasa.gov)

†currently at the University of California, Davis

††currently at the University of California, Berkeley

## Key Points:

-In the first 20 orbits of the Juno mission, over 150 waves and wave-like features have been detected by the JunoCam public-outreach camera.

-A wide variety of wave morphologies were detected over a wide latitude range, but the great majority were found near Jupiter's equator.

-By analogy with previous studies of waves in Jupiter's atmosphere, most of the waves detected are likely to be inertia-gravity waves.

43 Abstract

44

45 In the first 20 orbits of the Juno spacecraft around Jupiter, we have identified a variety of wave-  
46 like features in images made by its public-outreach camera, JunoCam. Because of Juno's  
47 unprecedented and repeated proximity to Jupiter's cloud tops during its close approaches,  
48 JunoCam has detected more wave structures than any previous surveys. Most of the waves  
49 appear in long wave packets, oriented east-west and populated by narrow wave crests. Spacing  
50 between crests were measured as small as ~30 km, shorter than any previously measured. Some  
51 waves are associated with atmospheric features, but others are not ostensibly associated with any  
52 visible cloud phenomena and thus may be generated by dynamical forcing below the visible  
53 cloud tops. Some waves also appear to be converging and others appear to be overlapping,  
54 possibly at different atmospheric levels. Another type of wave has a series of fronts that appear  
55 to be radiating outward from the center of a cyclone. Most of these waves appear within 5° of  
56 latitude from the equator, but we have detected waves covering planetocentric latitudes between  
57 20°S and 45°N. The great majority of the waves appear in regions associated with prograde  
58 motions of the mean zonal flow. Juno was unable to measure the velocity of wave features to  
59 diagnose the wave types due to its close and rapid flybys. However, both by our own upper  
60 limits on wave motions and by analogy with previous measurements, we expect that the waves  
61 JunoCam detected near the equator are inertia-gravity waves.

62

63 Plain Language Summary

64

65 The JunoCam camera aboard NASA's Juno mission to Jupiter has detected wave-like features  
66 over its 20 orbits that are smaller and more numerous than ever seen before in Jupiter's  
67 atmosphere. Most of the waves are in elongated wave packets, spread out in an east-west  
68 direction, with wave crests that are often perpendicular to the packet orientation; others follow  
69 curved paths. The space between wave crests can be as short as 30 kilometers. Some waves can  
70 appear close to other atmospheric features in Jupiter, while others seem to have no relationship  
71 with anything nearby. In one case, wave crests appear to be radiating outward from the center of  
72 a cyclone. Most waves are expected to be atmospheric gravity waves - vertical ripples that form  
73 in the atmosphere above something that disturbs air flow, such as a thunderstorm updraft,  
74 perturbations of flow around other features, or from some disturbance from below that JunoCam  
75 does not detect. JunoCam is uniquely qualified to make such discoveries, with its wide-angle  
76 field of view that delivers sweeping vistas of the giant planet's atmosphere as the spacecraft  
77 swoops within about 2,100 miles (3,400 kilometers) of Jupiter's cloud tops during each science  
78 pass.

79

80 Submitted to Journal of Geophysical Research - special issue on Juno results), 2019 December  
81 31.

82

## 83 1. Introduction

84

85 The Juno mission’s JunoCam instrument (Hansen *et al.* 2017), conceived as a public-  
86 outreach camera, has provided a surprising wealth of scientific results. These include the first  
87 close-up examination of Jupiter’s polar regions (Orton *et al.* 2017), in particular the unexpected  
88 presence and properties of constellations of cyclonic vortices around each pole (Adriani *et al.*  
89 2018a, Tabataba-Vakili *et al.* 2019). JunoCam’s proximity to Jupiter’s cloud tops has also  
90 provided high-resolution details of Jupiter’s Great Red Spot and its environment (Sánchez-  
91 Lavega *et al.* 2018). These studies have been enabled by JunoCam’s wide field of view ( $58^\circ$ )  
92 and the close proximity of the spacecraft to the clouds being imaged, with target distances as  
93 small as 3,500 km near closest approaches (“perijoves”), yielding a horizontal pixel-to-pixel  
94 spacing as good as 3 km.

95

96 We have used JunoCam’s coverage over a wide range of latitudes, coupled with its high  
97 spatial resolving power, to examine all of our images for various phenomena in Jupiter’s clouds.  
98 Small-scale waves, with wavelengths (distances between wave crests) less than  $\sim 300$  km, were  
99 first detected in 1979 by Voyager (Hunt and Muller, 1979) and have been detected by Galileo  
100 (e.g. Bosak & Ingersoll, 2002) and New Horizons (e.g. Reuter *et al.*, 2007) since then, as well as  
101 by the near-infrared JIRAM instrument on Juno (Adriani *et al.*, 2018; Fletcher *et al.* 2018).  
102 Larger waves, with scales of 1200 km or greater, have since also been detected from the Earth  
103 using Hubble Space Telescope (HST) and ground-based imaging (Simon *et al.*, 2018). A  
104 summary of observations of these waves is given in Table 1, which includes and updates similar  
105 information in Table 1 of Simon *et al.* (2015) and various tables in Simon *et al.* (2018). Table 1  
106 includes a JunoCam wave feature examined by Sánchez-Lavega *et al.* (2018) that we will also  
107 consider in this report. No waves were detected by the Cassini mission, most likely because  
108 Cassini was too far from Jupiter for adequate spatial resolution, but other reasons as possible.  
109 Virtually none were seen by Galileo imaging despite several close, although spatially limited,  
110 passes. The planet-encircling New Horizons waves were a surprise, as were the larger waves  
111 observed by HST and ground-based imaging for the past four years, which Cassini would have  
112 detected. During the Cassini epoch, there may not have been sufficient contrast to detect waves  
113 or waves were simply not propagating because of conditions unknown.

114

115 Below, we describe how the measurements are made, followed by a survey of the  
116 different types of atmospheric waves we have detected - along with any analogous wave  
117 formations in the Earth’s atmosphere. We then discuss quantitative properties of the waves and  
118 conclude with an analysis and discussion section.

119

120

## 121 2. Description of the measurements

122

123 JunoCam is a CCD-based camera, spanning a  $58^\circ$  field of view. The instrument is a  
124 “push-frame” imager, taking advantage of Juno’s 2 RPM spin to sweep its  $58^\circ$  swath to build  
125 spatial and spectral coverage without involving a shuttering mechanism. Thus, sequential  
126 images are acquired in broadband blue, green and red filters plus a narrow-band filter centered

127 on a 889-nm methane absorption band. Time-delayed integration of multiple pixel rows builds  
128 up the signal-to-noise ratio. Hansen *et al.* (2017) provide details of the instrument and its modes  
129 of operation. Sequential images are typically rendered in red-green-blue (“RGB”) composites,  
130 with the “methane filter” acquired and rendered separately, and the RGB images cover all  
131 latitudes on nearly all perijoves. The spatial resolution varies with the distance to the planet,  
132 which changes with each orbit: successive perijoves move approximately one degree of latitude  
133 north. For all the waves we discuss in this report, the spatial resolution is much finer than the  
134 distances reported in each case.

135  
136 In order to determine properties of the features, each image was transformed into a  
137 cylindrical cartesian map in longitude and latitude. This was done independently of the standard  
138 coordinate-transformation approach using the SPICE system (Acton 1996), as image timing,  
139 orientation in the spacecraft coordinate system and optics distortion were still being determined.  
140 We used limb fitting to constrain these properties, as the limb appears in all of our images.  
141 Current SPICE data show good agreement with these maps, with the limb-fitting approach  
142 showing an uncertainty better than  $2^\circ$  in the position of the south pole, as reported by Tabataba-  
143 Vakili *et al.* (2019). Further details of this mapping process are provided by Adriani *et al.* (2018:  
144 see their Supplementary Information) and by Tabataba-Vakili *et al.* (2019). All JunoCam  
145 images are publicly available on the Mission Juno web site:  
146 <https://www.missionjuno.swri.edu/junocam/processing>.

147  
148 Figure 1 shows an example of a full JunoCam image, rendered in a cylindrically mapped  
149 format, together with an excerpt (“crop”) of the image in which we identify wave-like features.  
150 The mapped versions were adjusted to compensate for the variation of illumination across the  
151 field. We found that a second-order power-law enhancement of color composites allowed wave  
152 features to be identified more readily. For the images shown below, as well as in the  
153 Supplemental Information, we further stretched each red, green and blue color independently for  
154 ease of identification by the reader. We also applied unsharp-mask sharpening in a few cases to  
155 make faint waves appear more prominently. Several coauthors independently searched manually  
156 through all of the JunoCam images in order to identify wave-like features that were candidates  
157 for this study. For detailed quantitative measurements, we used additional high-pass filtering to  
158 isolate fine-scale features. Our quantitative measurements are based on maps of the images  
159 rendered with 180 pixels per degree of latitude and longitude, together with high-pass filtering.  
160 We did not find identifiable wave features in any methane-band images. As a result, our  
161 discussion will be limited to enhanced RGB-composite images. We did not see any consistent  
162 differences in the contrast of wave features between the colors in images, which do not have any  
163 radiometric calibration.

164

## 165 3. Results

### 166 3.1 Overview.

167  
168 We limited the search for and characterization of waves to observations between  
169 perijoves 1 and 20 (2016 August 27 – 2019 May 29). Hereafter we will abbreviate “perijove” as  
170 “PJ”. During PJ2 (2016 October 19), no close-up images were made of Jupiter’s atmosphere as  
171

172 the result of a spacecraft “safing” event immediately before close approach. During PJ19 (2019  
173 April 6), JunoCam only took distant images of Jupiter, as a result of an unusual orientation of the  
174 spacecraft for most of that peri-jove in order to enable scanning in longitude by Juno’s  
175 Microwave Radiometer (MWR) instrument. The Supplemental Information to this report  
176 documents and illustrates all of the images in which we identified wave-like features with more  
177 than two wave fronts, together with a visual aid to identify the waves. In this report we select  
178 particular images that provide examples of the wide variety of waves and wave-like phenomena  
179 and their properties. The reader is free to observe all the images that are available in various  
180 processed forms on the Mission Juno web site in order to verify or refute our selections, as well  
181 as to identify potential additional candidates.  
182

### 183 3.2 Types of wave-like features. 184

185 Our survey of JunoCam images has revealed a surprising variety of features with wave-  
186 like morphologies. In order to be inclusive in our inventory, we include here (and in the  
187 Supplemental Information file) features with any regularly repeated patterns that are three or  
188 more in number. The survey below includes many features that have not been discussed  
189 previously in the context of atmospheric waves in Jupiter. They are presented in terms of  
190 differences in visual morphology, without implication that this differentiation arises from the  
191 associated responsible dynamics.  
192

193 3.2.1 Long wave packets with short, dark wave fronts represent 79% of the types of  
194 waves in our inventory, especially in the Equatorial Zone (EZ) that were also detected in  
195 previous studies, particularly from Voyager imaging (Table 1).

196 3.2.1.1. Orthogonal wave crests. Figure 2 shows two examples of these waves in which  
197 the wave front is more-or-less orthogonal to the direction of the wave packet. The morphology  
198 of the waves shown in Fig. 2 is most similar to those waves described in the articles cited in  
199 Table 1, although they are an order of magnitude smaller. They are most commonly referred to  
200 as mesoscale waves, by analogy to their appearance in the Earth’s atmosphere. Our search  
201 through JunoCam images (see the images in the Supplemental Information file) did not appear to  
202 sample any of the longer-wavelength (~1200-1900 km) packets detected by previous studies  
203 (Table 1), most likely as a result of the limited area over which JunoCam images can cover.

204 3.2.1.2. “Tilted” wave crests. Even more commonly, the detected packets have wave  
205 fronts that are not oriented orthogonally to the wavefront direction. Several examples of these  
206 “tilted” wave fronts are shown in Figure 3. Simon et al. (2015) stated that this is consistent with  
207 an interpretation of the waves as baroclinic instabilities that tilt northward and westward with  
208 altitude, as noted on a theoretical basis by Holton (1992) and by observations of waves in the  
209 Earth’s atmosphere (e.g. Blackmon et al. 1984). This implies that we are sensing the upper  
210 levels of such waves. Several images reveal the presence of large numbers of similar waves, as  
211 shown in the various panels of Figure 4. The waves are most often short with wave packets  
212 oriented east-west, although there are many wave packets not ostensibly oriented in any  
213 preferred direction (Fig. 4D). Some clearly cross one another, implying that the sources of their  
214 origin are not uniform. Simon et al. (2015b) argue that, if the waves are baroclinic instabilities,  
215 then their meridional extent depends on the Rossby radius of deformation, which they estimate  
216 as between 500 and 1400 km near the equator, which is where most of our detections of these  
217 waves lie. The Rossby radius of deformation is also where energy is transferred from small-

218 scale turbulence to zonal winds (see Salyk et al. 2006, Young and Read 2017). Since the mean  
219 of both meridional extent (~250 km on average) and wavelength (distance between wave crests,  
220 ~170 km), are much shorter than the Rossby deformation radius, it is logical to assume that they  
221 are formed by and interact with small-scale turbulence, and thereby propagate the waves in all  
222 directions. This is consistent with our observation that few, if any, of these waves are clearly  
223 associated with other atmospheric features.

224 3.2.1.3. Curved wave packets. Sometimes the short wavefronts are aligned in wave  
225 packets that themselves appear to be curved, are associated with larger features, and are not  
226 located in the EZ. Figure 5 shows two examples. Figure 5A shows the short wave-packets  
227 associated with the curved northern boundary of the Great Red Spot (GRS) near 15.8°S,  
228 described by Sánchez-Lavega et al. (2018). This is the first of two cases in which multiple  
229 images of waves were made, the result of intensive targeting of the GRS by Juno at PJ7.  
230 Sánchez-Lavega et al. (2018) estimated a phase speed for the wave of  $45\pm 20$  m/s relative to the  
231 very rapid local flow and determined that they were consistent with internal gravity waves, given  
232 estimates for the Richardson number for that part of the atmosphere that were based on the  
233 vertical wind shear deduced from temperature maps of the region (Fletcher et al. 2010). Two  
234 other examples of such wave packets imaged at PJ15 are shown. Figure 5B shows one on the  
235 south edge of a bright anticyclonic eddy in the NEB near 15.8°N, and Figure 5C shows one on  
236 the south edge of a dark cyclonic circulation in the SEB near 17.3°S. Just as for the wave trains  
237 in the northern edge of the GRS (Fig. 5A), these two wave packets are located on or near the  
238 peaks of retrograde (westward) flows that are probably accelerated in these locations because of  
239 the circulation.

240  
241 Another curved wavefront example is shown in Figure 5D: a dark, lobate feature with  
242 short wave crests that are most clearly detectable along its periphery. This feature is located in  
243 the chaotic region to the west of the GRS (see Fig. 6 for context). Interestingly, the entire chaotic  
244 region covers a much larger area to the northwest and west of the GRS, but these waves only  
245 appear in the region shown in Figure 5D. The dark part of this lobate feature appears only  
246 slightly brighter in 5- $\mu$ m radiance than its surroundings using contemporaneous NASA Infrared  
247 Telescope Facility (IRTF) observations. Thus, it is likely to be a region of very moderate dry  
248 downwelling that only partially clears out particles in cloud layers. Although the series of wave  
249 crests appears to line the sharply curved periphery of the dark feature, the crests are more likely  
250 to be roughly parallel streaks in a haze that overlies the entire region, with their visibility over  
251 the darker regions of this image strongly subdued. This interpretation is reinforced by studies of  
252 the winds from Juno-supporting observations by HST (Wong et al. 2020). Figure 6 shows the  
253 results of tracking winds in this region. Relative to the mean zonal winds, the residual winds  
254 shown in this figure appear to be flowing up toward the northwest along the dark lobe with  
255 speeds of  $65\pm 17$  m/s. Thus, the waves appearing in Fig. 5D are aligned with the local retrograde  
256 flow in high-shear regions. In this respect, they are similar to the curved wave packets described  
257 in the preceding paragraph.

258  
259 3.2.2. Short wave packets with wide wave fronts, shown in Figures 7 and 8, are also  
260 detected in our survey. In the Earth's atmosphere, such waves are often associated with  
261 thunderstorms producing a brief impulse period with radiating waves. Other curved features  
262 situated adjacent to each other are shown in the Supplemental Information file, which are shorter  
263 and difficult to distinguish from different albedo clouds that are stretched along streamlines (see

264 Figs PJ05\_108, PJ14\_25a, PJ14\_25b, and PJ14\_25c.) Somewhat similar features were detected  
265 in a Voyager image of “spiral” waves to the west of a dark brown cyclonic feature commonly  
266 called a ‘barge’ (Simon et al. 2018). Although there is some overlap between these waves and  
267 those described in section 3.2.1 in a spectrum of the length-to-width ratio of waves, these waves  
268 appear to occupy a generally distinct locus in plot of the length vs width of waves (see Fig. SI3-2  
269 in the Supplemental Information).

270  
271 Other waves are even more distinct. The arrows in Figure 8 show extremely long, closely  
272 spaced parallel lines that could be waves. Just as for the wave packets illustrated in Figure 7,  
273 both are curved. The pair of lines indicated in the upper part of the figure appear to have no  
274 visual association with any nearby feature, although they are situated between the bright  
275 (possibly upwelling) spot to the north and the darker region to its south. This darker region is an  
276 extension (sometimes called a “festoon”) of a blue-gray region along the southern boundary of  
277 the North Equatorial Belt associated with bright 5- $\mu\text{m}$  radiances, called a “5- $\mu\text{m}$  hot spot”. The  
278 narrow dark lines indicated in the bottom of Figure 8 are close to the southern boundary of the  
279 dark festoon. Although they could simply be long streaks associated with streamlines of flow  
280 along the festoon, they appear to be particularly narrow and well defined with sharp edges,  
281 particularly at their eastern extents. This differentiates them particularly from far less distinct  
282 streaks along the northern boundary of the festoon. They are also accompanied by shorter crests  
283 that are aligned perpendicular to the length of the lines. These orthogonal waves are not  
284 explicitly indicated in Figure 8 by white grids in order to make the extent of the long lines  
285 clearer, but they are illustrated in the same region shown in the Supplemental Information file as  
286 Figure 20\_34a. Orton et al. (2017) detected linear features in the north polar region, but they  
287 were associated with the edge of a well-defined haze region whose boundary could be traced  
288 using the 890-nm “methane” JunoCam filter. JunoCam did not take images of the features  
289 indicated in Figure 8 with the 890-nm filter, and they are below the spatial-resolution limits of  
290 Earth-based imaging in similar filters. The closest morphological analogies in the Earth’s  
291 atmosphere might be roll clouds, formerly known as cumulus cloud streets, e.g. Yang and Geerts  
292 (2014), which are most often detached from but associated with a cumulonimbus base. These  
293 are now classified as volutus clouds (<https://cloudatlas.wmo.int/clouds-species-volutus.html>) by  
294 the International Cloud Atlas. Another possibility is that they represent a version of transverse  
295 cirrus clouds, identified in upper-level tropospheric structures in the Earth’s atmosphere (Knox et  
296 al.2010).

297  
298 3.2.3. Wave packets with bright features appear different from the waves indicated up to  
299 this point (Figs. 2-7), which are recognizable by their dark or alternating dark-to-light crests.  
300 JunoCam has imaged many waves and wave-like features that are manifested as regular, repeated  
301 patterns of bright clouds, visually similar to terrestrial water-based clouds. We presume that  
302 differences between darker and brighter wave crests could be the composition of the material  
303 affected. Possibly the waves themselves induce condensation of bright white clouds along their  
304 crests, similar to what was seen in the mid-NEB on much larger scales by Fletcher et al. (2017).  
305 This might imply differences in altitude, e.g. perturbations of an upper-tropospheric haze layer  
306 near 200-300 mbar (e.g. Sromovsky et al., 2017, and Braude et al. 2020) versus those of a  
307 condensate cloud, such as a layer of “cirrus”  $\text{NH}_3$  ice particles near the 600-mbar condensation  
308 level. This corresponds to an altitude difference near the equator of roughly 15-20 km, an  
309 interval on the order of or less than an atmospheric scale height.

310  
311  
312  
313  
314  
315  
316  
317  
318  
319  
320  
321  
322  
323  
324  
325  
326  
327  
328  
329  
330  
331  
332  
333  
334  
335  
336  
337  
338  
339  
340  
341  
342  
343  
344  
345  
346  
347  
348  
349  
350  
351  
352  
353  
354  
355

Figure 9 shows a variety of examples of regular spacings between light-colored clouds detected by JunoCam. We lack the means to determine whether dark regions adjacent to lighter ones simply represent lower-albedo regions that are relatively cloudless or actual shadows of the brighter clouds. One likely exception to this are the clouds associated with the wave packet in the upper-left area of Figure 9A, which appear similar to terrestrial cirrocumulus clouds that have shadows associated with them. (If all of the dark area to the right of the largest dark region is a shadow, then the height of the largest cloud relative to the region around the cloud is on the order of 10 km.) We repeat the caveat of Simon et al. (2015) that such dark features may not be shadows but local regions of aerosol clearing “as atmosphere parcels rise and ices condense out to make the wave crests”. The clouds in the other panels are often arranged in a straight line or a segmented straight line with cirrus-like wisps trailing away from them. Figure 10 shows other regular patterns of bright clouds that are associated with narrower white features. The narrow meridional extent of these clouds (~150 km or less) is potentially the result of a very meridionally constrained flow. We note that both are curved and could be associated with constraining wind flows.

Figure 11 shows four instances of very bright, discrete clouds forming regular, extended patterns. These clouds extend to higher altitudes than their surroundings, as evidenced by shadows that often accompany them. Individual clouds such as these appear in various locations elsewhere in the planet, and we will describe and analyze them as a class in a separate report. We include this subset of them in our description of a distinct type of wave. Figure 11A shows a close up of such clouds, an expanded portion of Fig. PJ04\_103b in the Supplemental Information file. A wave packet can be seen that appears to be controlling small, bright cloud features. These are located in a bright patch that is part of a complex system of upwelling disturbances in the North Equatorial Belt (NEB), also known as ‘rifts’. Figure 11B shows a weak anticyclonic feature, in the center of which is a central bright cloud, accompanied to its southeast through southwest by short linear arrays of similar bright clouds. Two are shown with white grids that indicate individual cloud features that are resolved. Figures 11C and 11D also show individual clouds that comprise a wave packet, similar to the linear packet shown in Figure 11A. In Figure 11C, the clouds appear like balls or small smears, whereas in Figure 11D they appear like C-shaped arcs. If the dark regions accompanying the clouds in Figs. 11B, 11C and 11D are shadows, it would imply that they are clouds whose tops are higher than the surrounding darker cloud deck. Based on the incident angle of illumination, we estimate from the length of its shadow that the central cloud in Fig. 11B is only 3-4 km above the surrounding cloud deck. A similar estimate for the range of shadow lengths associated with various bright clouds in Fig. 11C implies that they are 5-12 km above the surrounding cloud deck. From the shadows associated with several C-shaped arcs in Fig. 11D, we estimate that they rise as much as 6-13 km above the background cloud deck. There are other similar features in both Figs. 11C and 11D, but they are not fully resolved. Although we cannot determine with absolute certainty that these clouds extend down to the level of the surrounding cloud deck, that is the impression one gets if the accompanying dark regions are interpreted as shadows. If these bright clouds do extend vertically downward to the surrounding cloud deck, then they appear less like linear versions of stratiform clouds on the Earth, than a series of upwelling cumulus clouds in which the intervening spaces between them simply represent regions of compensating subsidence.

356 3.2.4. Lee waves are stationary waves generated by the vertical deflection of winds over  
357 an obstacle, such as a mountain, a thermal updraft or a vertical vortex. Unlike the Earth, there  
358 are no mountains in Jupiter’s atmosphere, but there may indeed be the dynamical equivalent. If  
359 the long streaks in Figure 12 that stretch diagonally (upper left to the lower right) in the figure  
360 are tracking streamlines associated with local winds, and the winds are moving from the  
361 northwest to the southeast (upper left to the lower right in the figure), then the lee wave is the  
362 three-wavefront feature indicated by the white grid lines that is orthogonal to the flow. This  
363 requires that the local winds are passing not only around the bright upwelling anticyclonic vortex  
364 in the upper left of the frame, but also over it, consistent with very subtle streaks seen over the  
365 bright vortex. We note that not only the three waves indicated but also the lines that appear to be  
366 tracing the wind flow are elevated above the background cloud field, as marked by the shadows  
367 on their eastern sides. The most prominent of the shadows is on the eastern side of the central  
368 wave, the length of which implies that the peak of the wave is some 10 km about the background  
369 cloud deck. This is, in fact, the only example of such a wave in our survey. One reason could be  
370 that other atmospheric features are too high to permit flow over them, compared with the  
371 relatively young anticyclonic vortex in Figure 12.

372  
373 3.2.5. Waves associated with large vortices are shown in Figure 13. Figure 13A shows a  
374 very compact cyclonic feature with a set of extended radial wavefronts in the North Equatorial  
375 Belt. These resemble similar structures in terrestrial cyclonic hurricanes. The waves delineated  
376 in Figure 13A show morphological similarities to “transverse cirrus bands” (hereafter ‘TCB’)  
377 identified in upper-level tropospheric structures on Earth (Knox et al. 2010). TCB are defined by  
378 the American Meteorology Society as “*Irregularly spaced bandlike cirrus clouds that form*  
379 *nearly perpendicular to a jet stream axis. They are usually visible in the strongest portions of the*  
380 *subtropical jet and can also be seen in tropical cyclone outflow regions.*” (American  
381 Meteorological Society 1999). TCBs are also frequently observed in midlatitude mesoscale  
382 convective systems (MCS) and in extra-tropical cyclones. Numerical studies (Trier et al. 2010,  
383 Kim et al. 2014) have successfully replicated these cloud features and therefore have provided  
384 insight to their formation. Currently, there is no consensus regarding the dynamics responsible  
385 for TCB in all their observed forms (Knox et al. 2010). Multiple interacting factors that have  
386 been implicated in the genesis of these features, including gravity waves, Kelvin-Helmholtz  
387 instabilities, weak or negative moist static stabilities, and vertical wind shears (Dixon et al. 2000,  
388 Trier et al. 2010, Knox et al. 2010).

389  
390 There are some common characteristics that TCB share in the Earth’s atmosphere. First,  
391 the bands frequently originate in a region of anticyclonic vorticity, positive divergence, and in  
392 weak or negative static stability (Trier et al. 2010). Second, the majority of the bands appear in  
393 regions of strong relative vorticity gradient, and often persist beyond the life of the originating  
394 MCS (Lenz 2009). Third, the bands are often oriented along the vertical wind gradient, which  
395 provides surprising evidence they share some dynamical characteristics with boundary-layer  
396 horizontal convective roll vortices (Trier et al 2010, Kim et al. 2014), commonly observed on  
397 Earth as cloud streets (Yang & Geerts 2006). Fourth, there is evidence that gravity waves  
398 propagating below the cirrus cloud deck, the release of latent heat within the bands, and  
399 longwave cooling above and longwave warming below the bands appears to favor the formation  
400 of TCB. In addition to Figure 13A, the wave-like features shown in Figs. 2A, 3D, 4A, 5, 9A,  
401 and 9C appear similar to terrestrial TBC. Although it is difficult to know if they are true analogs

402 in the absence of detailed horizontal wind measurements of these clouds (as well as temperature  
403 measurements to understand the 3D wind gradients), their morphologies are suggestive. If this is  
404 the case, then complex small-scale dynamics may be operating in and below the Jovian ammonia  
405 cloud deck not dissimilar to those on Earth.

406  
407 The wave features in Figure 13A bear some resemblance to similar features found in  
408 tropical cyclones. Animations of tropical cyclones show high-frequency circular gravity waves in  
409 the central dense overcast cirrus shield ('CDO', Molinari et al. 2014) emanating from vigorous  
410 convection in or near the eyewall. Perhaps more relevant to the appearance of the features in  
411 Figure 13A, radial-aligned TCB are also commonly observed as 'spokes', which are more or less  
412 oriented orthogonally to the gravity waves. In many cases, the circulation of the parent vortex  
413 twists the spokes to appear like the teeth of a circular saw blade or as long thin curved filaments.  
414 In addition, shallow-water numerical modeling of vortex dynamics using the Explicit Planetary  
415 Isentropic Coordinate (EPIC; Dowling et al. 1998) in Brueshaber et al. (2019) also display  
416 curved wave-like features similar to those in Figure 13A, but their waves are certainly due to  
417 gravity waves formed during the merger of like-signed vortices for which we have no direct  
418 evidence in this figure.

419  
420 On the other hand, for the much larger anticyclonic white oval in Figure 13B, it is  
421 possible that the curved cloud features appearing there to be a manifestation of gravity waves.  
422 The spatial resolution of this image is sufficient to see both the internal spiral structure of the  
423 white oval and a regular set of dark bands extending to its exterior. Anticyclones on Jupiter, such  
424 this one, often feature a high-speed 'collar' surrounding a calmer interior (e.g., Marcus 1993).  
425 The shear of the high-speed wind against slower winds outside of the vortex may be sufficient to  
426 generate a Kelvin-Helmholtz wave, which may explain the scalloped appearance of the white  
427 clouds adjacent to the surrounding red clouds.

428  
429  
430 3.2.6. Long, parallel dark streaks are detectable at mid-latitudes. Long streaks are seen in many  
431 areas of Jupiter's cloud system, usually with a non-uniform and chaotic pattern (e.g. the diagonal  
432 ones in Fig. 12). But, as shown in Figure 14, some are seen in very regularly spaced parallel  
433 bands. In several cases, the parallel banding is not only regularly spaced but sinusoidal in  
434 behavior, with a distance between crests ranging between 280 and 360 km. All such features  
435 are detected far from the equator. Their orientation suggests that they are tracing out the direction  
436 of flow on streamlines, in often complicated patterns, with lengths from 500 km to 3800 km (an  
437 upper limit that may be constrained by JunoCam's field of view). Almost all of the parallel  
438 streaks in the examples shown in Fig. 14 are associated with larger atmospheric features,  
439 although those features do not appear to be located where the streaks originate. In Figure 14A,  
440 one set of these appears to be 'flowing' around an anticyclonic vortex in the lower left. It and a  
441 set of streaks in the center of the feature have topography, with shadows apparent on their  
442 eastern sides. In Figure 14B, long streaks possibly are associated with streamlines 'flowing'  
443 around small, red anticyclonic vortices. The NTB was very turbulent at the time of these  
444 observations, following a great disturbance in the preceding months (see Sánchez-Lavega et al.  
445 2017). A semi-transparent triplet of short, dark bands in the top left of this figure can be seen  
446 lying across longer bands that appear to be tracing wind flow. Figure 14C shows parallel streaks  
447 located between a weak cyclonic eddy on the left and a bright wave-like streak aligned with the

448 SEBs retrograde jet, at the bottom edge of the panel. Figure 14D shows several parallel cloud  
449 streaks in this turbulent part of the North North Temperate Belt (NNTB). Some are associated  
450 with the small cyclonic vortex in the lower right side of the panel. Often, the streaks appear to  
451 be on top of other features, implying that they represent flow that is manifested in a haze layer  
452 overlying deeper cloud layers. The best analog to these features lies not in the Earth's  
453 atmosphere but in Saturn's. Ingersoll et al. (2018) examine high-resolution images of Saturn's  
454 clouds taken during the Cassini mission's "proximal orbits". Their Figure 3 shows a flow around  
455 a vortex that is very similar to one around the vortex in Figure 11A. For their similar "thread-  
456 like filamentary clouds", they suggest that the implied laminar flow implies extremely low  
457 values of diffusivity and dissipation, which further quantitative analysis of these observations  
458 may verify is the case for these scales in Jupiter, as well.

459  
460 3.2.7. Unusual features are shown in Figure 15, which we might classify as waves only in the  
461 most general sense. Figure 15A shows a series of features with a regular spacing: three curved  
462 wavefronts next to an unusual series of relatively dark ovals indicated by the arrows. The dark  
463 ovals may be connected dynamically to the wavefronts, because they continue in the same  
464 direction and have roughly the same wavelength. The morphology of the three wave fronts  
465 implies that flow is from the northwest. We do not see an array of short, dark, curved lines  
466 elsewhere, so their spatial association with each other is extremely unusual. They are located  
467 near the boundary between the turbulent northern component and the smooth, orange southern  
468 component of the North Temperate Belt. Figure 15B shows a limited series of repeated patterns  
469 along the southern edge of an unusual white band located at the turbulent boundary between the  
470 northern and southern components of the North Temperate Zone. This short sequence bears  
471 some resemblance to a Karman vortex street, although one that may be dissipating or disrupted.

472  
473

### 474 3.3 Quantitative measurements of wave properties.

475  
476  
477

#### 477 3.3.1. Measurements of meridional distribution and size properties.

478  
479  
480  
481  
482  
483  
484  
485

479 Measurements were made of physical properties of all of the waves and wave-like  
480 features discussed. A table of all of these is available in the Supplemental Information file.  
481 Features are identified by Perijove and File number. Measured quantities are: the number of  
482 waves, the mean System-III longitude, mean planetocentric latitude, length and width of the  
483 wave train, the mean wavelength (distance between crests) and the tilt of the wave with respect  
484 to the orientation of the wave packet.

486 Figure 16 shows a histogram of the occurrence of waves as a function of latitude. In  
487 order for the reader to distinguish between different classes of wave-like features, some of which  
488 are arguably not propagating waves, we have separated out the different types of waves by  
489 morphology as discussed in the preceding sections. Table 2 shows our count of the different  
490 categories of waves. The overwhelming majority of wave-like features are clustered between  
491 7°S and 6°N latitude, the relatively bright EZ. These features are dominated by long wave  
492 packets with short wave crests, the type of waves detected by Hunt and Muller (1979) and  
493 discussed by Simon et al. (2015a) as mesoscale waves observed at low latitudes by previous

494 imaging experiments. These waves fall within the relatively bright EZ and appear to be sub-  
495 clustered with fewer waves between 1°S and the equator than between either 7°S and 1°S or the  
496 equator and 6°N. The next most populous category are waves with short packet lengths and long  
497 crests, which appear to be distinct not only because they appear to be clustered differently in  
498 length vs. width ratios, but also because they mostly populate latitudes between 1°N and 3°N.  
499 Waves that are generally associated with or influenced by larger features, most often associated  
500 with curved wave packets, are the next most abundant feature. These include the curved wave  
501 packets at the northern boundary of the GRS (Fig. 5A), the wave packets on the southern edge of  
502 a cyclonic circulation in the SEB (Fig. 5b) and on the southern edge of an anticyclonic eddy (Fig.  
503 5C), wave packets associated with the lobate feature in the chaotic region west of the GRS (Fig.  
504 5D), and parallel stripes near a weak eddy (Fig. 14C). All are located in regions of retrograde  
505 flow, as shown in Figure 17. All other types of features are detected less frequently (Table 2)  
506 and are scattered in the northern hemisphere. No waves of any type were detected south of 7°S  
507 other than the ones between 17°S and 20°S that are associated with larger features. There may be  
508 a small selection effect associated with the observations, since latitudes in the northern  
509 hemisphere are observed with an average spatial resolution that is higher than in the southern  
510 hemisphere, arising from the fact that the Juno spacecraft perijove is in the northern hemisphere  
511 and moving northward by about a degree of latitude for each successive, highly elliptical orbit.  
512 Perijove latitudes ranged from 3.8°N for PJ1 to 20.3°N for PJ20. Arguing against this is the fact  
513 that waves were detected in the southern hemisphere with wavelengths between 70 km and 200  
514 km, meaning that waves of this size range would have been detectable elsewhere if they were  
515 present. Such waves might, in fact, be present but undetectable if the hazes making them visible  
516 in the northern hemisphere were not present in the southern hemisphere outside the EZ, for some  
517 reason.

518  
519 Is the observed distribution of waves associated with other indicators of upwelling or  
520 turbulence? Clearly the preponderance of waves in the EZ is not correlated with the frequency  
521 of lightning detections, as no detections of lightning have been associated with that region, either  
522 historically (e.g. Borucki & Magalhães 1992, Little et al. 1999, Dyudina et al. 2004) or in the  
523 broad survey by the Juno Microwave Radiometer (Brown et al. 2018) that is sensitive to  
524 lightning discharges in the EZ (Juno’s Waves instrument, Imai et al. [2018] could not detect  
525 lightning in the EZ because the field lines do not reach Juno’s orbit.). The presence of water ice  
526 is one indirect measure of upwelling, and its detection from Voyager IRIS data by Simon-Miller  
527 et al. (2000) revealed a distribution that included the EZ but was significantly higher at latitudes  
528 south of ~10°S. This is consistent with our results only in the limited sense that several waves  
529 were associated with the GRS and its surroundings. Another indirect measure is the presence of  
530 pristine ammonia ice, as measured most recently by New Horizons (Reuter et al. 2007), which  
531 determined that spectrally identifiable ammonia clouds (SAICs) occurred “near active storms or  
532 upwelling regions”, which includes some regions in the EZ and is more broadly consistent with  
533 several of our specific observations at higher latitudes. New Horizons did not detect SAICs near  
534 the GRS, as the typically chaotic region to its northwest was not active during the New Horizons  
535 encounter. From the Juno mission itself, the striking deep column of concentrated ammonia at  
536 2°N to 5°N detected by the Microwave Radiometer (MWR) instrument implies upwelling (Li et  
537 al. 2017, Bolton et al. 2017), which is consistent with the concentration of waves there. This is  
538 consistent with contemporaneous ground-based observations (de Pater et al. 2019, Fletcher et al.  
539 2016, 2020). However, we detected an equal number of waves in the southern component of the

540 EZ, where there was not nearly as great a concentration of ammonia gas, so this particular  
541 correlation is imperfect. We note that from studies of cloud properties from reflected sunlight,  
542 the full EZ is known as a region in which tropospheric clouds and hazes extend higher than other  
543 locations on the planet outside the GRS, as evidenced by the general concentration of upper-  
544 atmospheric opacity historically (e.g. West et al. 1986) and in more recent work (see Figs. 4 and  
545 12 of Sromovsky et al. 2017, Fig 13B of Braude et al. 2020) or by the distribution of  
546 disequilibrium constituents (see Fig. 4 of Orton et al. 2017b). This is consistent with the entire  
547 EZ being a region of general upwelling.

548  
549 Figure 17 plots the distribution of mean wavelengths for different types of waves and  
550 wave-like features as a function of latitude, co-plotted with mean zonal wind velocity. The  
551 minimum distance between crests is 29.1 km for the spacing between the discrete white features  
552 shown in Fig. 10A. Not significantly larger is the 30.9 km between crests of waves in a low-  
553 latitude long wave packet with short crests. These values are available in Table 1 of the  
554 Supplementary Information file. The variability of wavelengths within a single packet is  
555 typically no greater than 20-30%. The equatorial waves with long packets and short crests in the  
556 EZ have wavelengths that are clustered between 30 km and 320 km, with most between 80 and  
557 230 km in size. The bimodal appearance of the distribution of EZ waves is not consistent with  
558 the distribution of waves detected from Voyager (Simon et al. 2015a), which also has several  
559 wave packets distributed at latitudes south of the EZ (see Figure 17). Similar to our study, most  
560 of these are associated with the GRS. Similar to Voyager, all the waves detected in JunoCam  
561 images in regions of retrograde flow are associated with discrete atmospheric features, such as  
562 the GRS. The virtual absence of waves observed in Voyager images covering the northern  
563 hemisphere is ostensibly the opposite of what we observe with JunoCam, although the key in  
564 Figure 16 shows that many of the wave-like features in the northern hemisphere might not have  
565 been categorized as waves by Voyager investigators.

566  
567 3.3.2. Measurements of wave phase speed.

568 The most diagnostic criterion between different types of waves is the propagation speed.  
569 The waves in the EZ were discovered by Voyager 1 and described by Hunt & Muller (1979),  
570 who found them to have low or zero speeds relative to their surroundings (whether in a plume  
571 tail or equatorial clouds). Simon et al. (2015b) also found little relative motion for these waves  
572 in Voyager 2 and Galileo Orbiter images. Arregi et al.(2009), studying Galileo Orbiter images,  
573 likewise found no measurable relative motion for waves on the equator, but a phase velocity of  
574 35 (+/-8) m/s for waves at 3°S. Simon et al. (2015b) adopted the conclusions of Flasar &  
575 Gierasch (1986), Bosak & Ingersoll (2002) and Arregi et al. (2009) that these waves detected by  
576 Voyager and Galileo images were best classified as inertia-gravity (IG) waves, a conclusion we  
577 do not revisit here. On the other hand, Simon et al. (2015b) differentiated the waves detected by  
578 New Horizons as Kelvin waves from those by Galileo and Voyager as IG waves on the basis of  
579 their phase velocity, crest length, and location; they measured a non-zero velocity ( $80\pm 5$  km/s)  
580 relative to the local zonal wind for the Kelvin waves that are confined to the equator compared  
581 with the IG waves, which are near stationary (upper limits to the phase velocity of 40 m/s or  
582 less). Unfortunately, the Juno spacecraft and orbit configuration that provides such close-up  
583 observations of Jupiter's clouds strongly limits our ability to determine velocities, and regions  
584 are rarely observed at adequate spatial resolution more than once per perijove. Subsequent  
585 perijoves typically observe longitudes that are far from the preceding one. Observations of the

586 Great Red Spot in PJ7 are one exception (Sánchez-Lavega et al. 2018), as noted above. Another  
587 is the circulation associated with a large cyclonic feature observed by both JunoCam and ground-  
588 based facilities (Iñurriagarro et al. 2020).

589  
590 We made another attempt in PJ20 to observe one region several times during a perijove,  
591 focusing on the northern component of the EZ, Images 33 through 37 (formally  
592 JNCE\_2019043\_20C00033\_V01 through JNCE\_2019043\_20C00037\_V01). We examined  
593 these quite carefully using a recently developed upgrade in our geometric calibration, which used  
594 limb-crossing times to correct for otherwise undetected errors in the data-acquisition timing.  
595 The results showed no change in the location of waves (marked in Fig. PJ20\_34a in the  
596 Supplemental Information file near 27.5°W longitude and 0.5°N latitude) over the 6 min, 4-sec  
597 interval between the first and last images of this sequence. We quantify this using a very  
598 conservative standard of 2 pixels for the pointing uncertainty, equivalent to 14 km for Image 33  
599 and 18 km for Image 37 – a linear dependence on the distance of the spacecraft from the waves.  
600 Using 16 km as an estimate of the mean displacement, this is equivalent to an upper limit for the  
601 phase speed of 44 m/s, a value consistent with a supposition that these are IG waves.

602  
603 Moreover, based on morphology alone, the New Horizons waves were slightly curved,  
604 had a consistent distance between wave fronts of  $305\pm 25$  km, a wave train that spanned the  
605 entire visible equator (more than 200,000 km in packet length), and were centered at the equator,  
606 spanning  $\pm 2^\circ$  in latitude (see Figs. 1 and 2 of Simon et al. 2015). The waves that we detected  
607 here have a broad range of wavelengths and crest lengths, are located at latitudes significantly far  
608 from  $\pm 1.5^\circ$  of the equator, and many wave packets are very short. Therefore, we suggest that  
609 these types of waves detected in JunoCam images, more similar to those seen in Voyager and  
610 Galileo observations, are most likely to be IG in origin.

## 611 612 4. Conclusions and future work

613  
614 Juno’s public-outreach camera, JunoCam, detected a plethora of waves or wave-like  
615 features in its first 20 perijove passes. Of these 157 features, 100 are waves with long, somewhat  
616 linear packets and short crests are identified as mesoscale waves, consistent with earlier studies.  
617 Many of these have wave crests that are nearly orthogonal to the wave packet orientation,  
618 although others that were tilted compared with this orientation. Another 25 wave packets were  
619 detected with short packets and long crests. As a group, they are likely to be features that are  
620 truly propagating waves. They are more in number than was detected by Voyager imaging in  
621 1979, and they include waves that are smaller in wavelength than any detected by previous  
622 missions. These waves form the vast majority of features detected in this study, and they are  
623 concentrated in a latitude range between 5°S and 7°N. Short wave packets often appear in several  
624 different orientations and sometimes overlap one another. Almost none of these appear to be  
625 associated with other features except for waves that appear to be oriented in lines of local flow,  
626 including packets with crests that appear darker than the local background or with bright  
627 features. These bright features appear both as discrete, tall clouds with shadows that imply they  
628 are higher than the background darker cloud deck, and simply as brighter features that have  
629 wispy “tails” and are connected to one another by an equally bright but narrow, elongated cloud.  
630 The difference between wide and narrow packets is presumably related to the width of the flow  
631 that is responsible for the wave. There were fewer waves in the EZ between the equator and

632 1°N than there were immediately north and south of this band, which was different from the  
633 waves detected by Voyager imaging in 1979 that were more equally distributed.  
634

635 Other waves, prominently those outside the EZ, are clearly associated with or influenced  
636 by other features. These include short-crested packets following the slightly curved path at the  
637 northern extent of the GRS, others associated with an anticyclonic eddy in the NEB and a  
638 cyclonic circulation in the SEB, and one associated with the turbulent flow west of the GRS.  
639 Three lee waves were detected in the wake of an upwelling anticyclonic vortex that were some  
640 10 km above the surrounding cloud deck. More features were detected that had repeated, wave-  
641 like features but may not represent propagating waves. Some of the linear arrangements of  
642 discrete white clouds followed the edges of vortices; although regular in spacing, these features  
643 may not represent propagating waves so much as alternating positions of upwelling and  
644 subsiding vertical flows. Several features appeared within or emanating from vortices. Two sets  
645 of extremely long, curved features were detected near the edges of a southwestern extension of a  
646 dark blue-gray region associated with high 5- $\mu\text{m}$  radiances at the southern edge of the NEB.  
647 Long, sinuous parallel streaks were detected, some with nearly sinusoidal lateral variability, that  
648 were analogous to features observed by the highest-resolution imaging of Saturn's atmosphere  
649 by Cassini (Ingersoll et al. 2018). No waves were detected south of 7°S that were not associated  
650 with larger vortices, such as the GRS. No waves or wave-like features were detected in regions  
651 of retrograde mean zonal flow that were not associated with larger features, similar to the waves  
652 detected by Voyager imaging.  
653

654 We had limited opportunities to classify waves on the basis of phase speed. Sánchez-  
655 Lavega et al. (2018) determined that the waves located at the northern extent of the GRS were  
656 internal gravity waves from their propagation speed with respect to the local flow, based on a  
657 displacement over a 9-minute interval between initial and final images. (Internal gravity waves  
658 are similar to IG waves but where Coriolis forces are not considered to be important.) JunoCam  
659 seldom observes features more than once, and usually with insufficient time to note a  
660 displacement. Our attempt to observe features in the EZ on PJ20 resulted in a 6-minute interval  
661 over which no motions were detected for equatorial features, providing an upper limit of wave  
662 motions that was not inconsistent with inertia-gravity waves. However, the waves detected in  
663 the EZ were not located directly at the equator, which bounded the Kelvin waves detected by  
664 New Horizons imaging (Simon et al. 2015b). Otherwise, the waves detected in the EZ are  
665 morphologically similar to those detected by Voyager, which Simon et al. (2015b) classified as  
666 inertia-gravity waves. These waves may well be associated generally with the upwelling winds  
667 that characterize the EZ.  
668

669 Work will continue to document and detect waves and wave-like features in Jupiter's  
670 atmosphere, including further attempts to examine regions over longer time intervals, although  
671 we note that observations of waves in the EZ will be lower in spatial resolution as the latitude of  
672 successive perijoves migrates northward by about 1° per perijove. We will also look for  
673 simultaneous measurements of waves in the near infrared by the JIRAM experiment to provide  
674 some constraints on the altitude of these features, which were otherwise only loosely constrained  
675 by occasional measurements of associated shadows. Furthermore, we expect that we and others  
676 will use these observations as a motivation to engage in comparisons with terrestrial analogs and  
677 numerical simulations that will further our understanding of the origin of these features and their

678 implications for the dynamics of Jupiter's atmosphere at these small scales and their relation to  
679 the larger picture of planetary dynamics at depth.

## 680 5. Acknowledgements

681  
682 Levin, Orton, Sinclair and Tabataba-Vakili were supported by funds from NASA distributed to  
683 the Jet Propulsion Laboratory, California Institute of Technology. Bolton and Hansen were  
684 supported by funds from NASA to the Southwest Research Institute and to the Planetary Science  
685 Institute, respectively. Brueshaber was supported by Western Michigan University's Dissertation  
686 Completion Fellowship. Ravine and Caplinger were supported by funds from NASA to Malin  
687 Space Science Systems. Fletcher is a Juno Participating Scientist supported by a Royal Society  
688 Research Fellowship and European Research Council Consolidator Grant (under the European  
689 Union's Horizon 2020 research and innovation program, grant agreement No 723890) at the  
690 University of Leicester. Wong was supported by NASA's Juno Participating Scientist program;  
691 a part of his contribution was based on observations from program GO-14661, made with the  
692 NASA/ESA Hubble Space Telescope, obtained at STScI, which is operated by AURA under  
693 NASA contract NAS5-26555. Nicholson was supported by NASA funds to the Jet Propulsion  
694 Laboratory as a participant in Caltech's Summer Undergraduate Research Fellowship (SURF)  
695 program at JPL. Thepenier and Anthony were participants in JPL's Student Independent  
696 Research Internship (SIRI) program.

697  
698 All the images used in this study are available for direct download from the Mission Juno site:  
699 <https://www.missionjuno.swri.edu/>

700  
701 We note that preliminary results, including a version of Figure 11, were included in a NASA  
702 press release: <https://www.jpl.nasa.gov/news/news.php?feature=7264>.

703  
704 © 2019 All rights reserved.

## 705 References

- 706  
707 Acton, C. H. 1996. Ancillary data services of NASA's navigation and ancillary information  
708 facility. *Planet. Space Sci.* 44, 65-70.
- 709 Adriani, A., Mura, A., Orton, G., Hansen, C., Altieri, F., Moriconi, M. L., Rogers, J., Eichstädt,  
710 G., Momary, T., Ingersoll, A., Filacchione, G., Sindoni, G., Tabataba-Vakili, F., Dinelli, B.  
711 M., Fabiano, F., Bolton, S. J., Connerney, J. E. P., Atreya, S. K., Lunine, J. I., Tosi, F.,  
712 Migliorini, A., Grassi, D., Piccioni, G., Noschese, R., Cicchetti, A., Plainaki, C., Olivieri, A.,  
713 O'Neill, M. E., Turrini, D., Stefani, S., Sordini, R., Amoroso, M. (2018a) Clusters of cyclones  
714 encircling Jupiter's poles. *Nature*. 555, 216-219. doi 10.1038/nature25491.
- 715 Adriani, A., Moriconi, M. L., Altieri, F., Sindoni, G., Ingersoll, A. P., Grassi, D., Mura, A.,  
716 Atreya, S. K., Orton, G., Lunine, J. I., Fletcher, L. N., Simon, A. A., Melin, H., Tosi, Ciccetti,  
717 A., Noschese, R., Sordini, R., Levin, S., Bolton, S., Plainaki, C., Olivieri, A. (2018b).  
718 Characterization of mesoscale waves in the Jupiter NEB by Jupiter InfraRed Auroral Mapper  
719 on board Juno. *Astron. J.* **156**, 246 (12pp).
- 720 American Meteorological Society (1999). Glossary of Meteorology, 2<sup>nd</sup> edition, American  
721 Meteorological Society: Boston, MA.

722 Allison, M. (1990). Planetary waves in Jupiter's equatorial atmosphere. *Icarus* 83, 282-307.

723 Arregi, J., Rojas, J. F., Hueso, R., Sanchez-Lavega, A. (2009) Gravity waves in Jupiter's  
724 equatorial clouds observed by the Galileo orbiter. *Icarus* 202, 358-360.

725 Blackmon, M.L., Lee, Y.-H., & Wallace, J. A. (1984) Horizontal structure of 500 mb height  
726 fluctuations with long, intermediate and short time scales. *J. Atmos. Sci.* 41, 961.

727 Bolton, S. J., Adriani, A., Adumitroaie, V., Anderson, J., Atreya, S., Boxham, J., Brown, S.,  
728 Connerney, J. E. P., DeJong, E., Folkner, W., Gautier, D., Gulkis, S., Guillot, T., Hansen, C.,  
729 Hubbard, W. B., Iess, L., Ingersoll, A., Janssen, M., Jorgensen, J., Kaspi, Y., Levin, S. M., Li,  
730 C., Lunine, J., Miguel, Y., Orton, G., Owen, T., Ravine, M., Smith, E., Steffes, P., Stone, E.,  
731 Stevenson, D., Thorne, R., Waite, J. (2017). Jupiter's interior and deep atmosphere: The first  
732 close polar pass with the Juno spacecraft. *Science* **356**, 821-825.

733 Borucki, W. J., Magalhães, J. A. (1992) Analysis of Voyager 2 images of Jovian lightning.  
734 *Icarus* 96, 1-14.

735 Bosak, T. and Ingersoll, A. P. (2002). Shear instabilities as a probe of Jupiter's atmosphere.  
736 *Icarus* 158, 401-409.

737 Braude, A. S., Irwin, P. G. J., Orton, G. S., Fletcher, L. N. (2020). Colour and tropospheric cloud  
738 structure of Jupiter from MUSE/VLT: Retrieving a Universal chromophore. *Icarus* 338 In press,  
739 doi: 10.1016/j.icarus.2019.113589.

740 Brown, S., Janssen, M., Adumitroaie, V., Atreya, S., Bolton, S., Gulkis, S., Ingersoll, A., Levin,  
741 S., Li, Cl., Li, L., Lu nine, J., Misra, S., Orton, G. Steffes, P., Tabataba-Vakili, F., Kolmasova,  
742 I., Imai, M, Santolik, O., Kurth, W., Hospodarsky, G., Gurnett, D., Connerney, J. (2018).  
743 Prevalent lightning sferics at 600 megahertz near Jupiter's poles. *Nature* 558, 87–90.  
744 doi.org/10.1038/s41586-018-0156-5.

745 Brueshaber, S., Sayanagi, K., M., Dowling, T. E. (2019). Dynamical regions of giant planet polar  
746 vortices. *Icarus* 323, 46-61. doi 10.1016/j.icarus. 2019.02.001

747 de Pater, I., Sault, R. J., Moeckel, C., Moullet, A., Wong, M. H., Goullaud, C., DeBoer, D.,  
748 Butler, B. J., Bjoraker, G., Adamkovics, M., Cosentino, R., Donnelly, P. T., Fletcher, L. N.,  
749 Kasaba, Y., Orton, G. S., Rogers, J. H., Sinclair, J. A., Villard, E. (2019) First ALMA  
750 millimeter-wavelength maps of Jupiter, with a multiwavelength study of convection.  
751 *Astrophys. J.* 158, 139 (17pp).

752 Dixon, R.S., Browning, K.A., Shutts, G.J. (2000). The mystery of striated cloud heads in satellite  
753 imagery. *Atmospheric Science Letters*, doi:10.1006/asle.2000.0001

754 Dyudina, U. A., Del Genio, A. D, Ingersoll, A. O., Porco, C. C., West, R. A., Vasavada, A. R.,  
755 Barbara, J. M. (2004). Lightning on Jupiter observed in the Ha line by the Cassini imaging  
756 science subsystem. *Icarus* 172, 24-36.

757 Flasar, F. M. and Gierasch, P. J. (1986). Mesoscale waves as a probe of Jupiter's deep  
758 atmosphere. *J. Atmos. Sci.* 43, 2683-2707.

759 Fletcher, L. N., Orton, G. S., Mousis, O., Yanamandra-Fisher, P., Parrish, P. D., Irwin, P. G. J.,  
760 Edkins, E, Baines, K. H., Line, M. R., Vanzi, T., Fujiyoshi, T., Fuse, T. (2010). Jupiter's Great  
761 Red Spot: High-resolution thermal imaging from 1995 to 2008. *Icarus* **208**, 306-328..

762 Fletcher, L. N. , Melin, H., Adriani, A., Simon, A. A., Sanchez-Lavega, A., Donnelly, P. T.,  
763 Antuñano, A., Orton, G. S., Hueso, R., Moriconi, M. L., Altieri, F., Sindoni, G. 2018. Jupiter's  
764 mesoscale waves observed at 5  $\mu\text{m}$  by ground-based observations and Juno JIRAM. *Astron. J.*  
765 **156**, 67 (13pp).

766 Fletcher, L. N., Greathouse, T. K., Orton, G. S., Sinclair, J. A., Giles, R. S., Irwin, P. G. J.,  
767 Encrenaz, T. (2016) Mid-infrared mapping of Jupiter's temperatures, aerosol opacity and

768 chemical distributions with IRTF/TEXES. *Icarus* 278, 128-161. doi  
769 10.1016/j.icarus.2016.06.008

770 Fletcher, L. N., Orton, G. S., Greathouse, T. K., Zhang, Z., Oyafuso, F. A., Levin, S. J., Li, C.,  
771 Bolton, S., Janssen, M., Mettig, H.-J., Rogers, J. H., Eichstädt, G., Hansen, C., Melin, H.,  
772 Grassi, D., Mura, A., Adriani, A. (2020). Jupiter's equatorial plumes and hot spots: Spectral  
773 mapping from Gemini/TEXES and Juno/MWR. *J. Geophys. Res.* (this issue).

774 Hansen, C., Caplinger, M. A., Ingersoll, Ravine, M. A., Jensen, E., Bolton, S., Orton, G. 2017.  
775 Junocam: Juno's outreach camera. *Space Sci. Rev.* 217, 475-506. doi:10.1007/s11214-014-  
776 0079-x.

777 Holton, J. R. 1992. An Introduction to Dynamic Meteorology (3<sup>rd</sup> ed.; New York; Academic  
778 Press).

779 Hunt, G. E., and Muller, J.-P. (1979). Voyager observations of small-scale waves in the  
780 equatorial region of the jovian atmosphere. *Nature* 280, 778-780.

781 Imai, M., Santolik, O., Brown, S., Kolmasova, IO., Kurth, W., Janssen, M., Hospodarsky, G.,  
782 Gurnett, D., Bolton, S., Levin, S. (2018). Jupiter lightning-induced whistler and sferic events  
783 with Waves and MWR during Juno perijoves. *Geophys. Res. Lett.* 45, 7268-7276.  
784 doi.org/10.1029/2018GL078864.

785 Ingersoll, A. P., Ewald, S. P., Sayanagi, K. M., Blalock, J. J. (2018). Saturn's atmospheres at 1-10  
786 kilometer resolution. *Geophys. Res. Lett.* 45, 7851-7856. doi.org/10.1029/2018GL079255.

787 Iñurriagarro, P., Hueso, R., Legarreta, J., Sánchez-Lavega, A., Eichstädt, G., Rogers, J. H., Orton,  
788 G. S., Hansen, C. J., Pérez-Hoyos, S., Rojas, J. F., Gómez-Forrellad, J. M. 2020. Observations  
789 and numerical modelling of a convective disturbance in a large-scale cyclone in Jupiter's South  
790 Temperate Belt. *Icarus*. **336**, 113475.

791 Kim, J.-H., Chun, H.-Y., Sharman, R.D., Trier, S.B. (2014). The role of vertical shear on aviation  
792 turbulence within cirrus bands of a simulated western Pacific cyclone. *Monthly Weather*  
793 *Review*, 142, 2794-2812.

794 Knox, J. A., Bachmeier, A. S., Carter, W. M., Tarantino, J. E., Paulik, L. C., Wilson, E. N.,  
795 Bechdol, G. S., Mays, M. J. (2010). Transverse cirrus bands in weather systems: a grand tour  
796 of an enduring enigma. *Weather* 65, 36-41.

797 Lenz, A., Bedka, K.M., Feltz, W.F., Ackerman, S.A. (2009). Convectively induced transverse  
798 band signatures in satellite imagery. *Weather and Forecasting*, 24, 1362-1373.

799 Li, C., Ingersoll, A., Janssen, M., Levin, S., Bolton, S., Adumitroaie, V., Allison, M., Arballo,  
800 A., Belotti, A., Brown, S., Ewald, S., Jewell, J., Misra, S., Orton, G., Oyafuso, F., Steffes, P.,  
801 Williamson, R. (2017). The distribution of ammonia on Jupiter from a preliminary inversion of  
802 Juno microwave radiometer data. *Geophys. Res. Lett.* **44**, 5317-5325.

803 Li, L., Ingersoll, A. P., Vasavada, A. R., Simon-Miller, A. A., Achterberg, R. K., Ewald, S. P.,  
804 Dyudina, U. A., Porco, C. C., West, R. A., Flasar, F. M. (2006). Waves in Jupiter's atmosphere  
805 observed by the Cassini ISS and CIRS instruments. *s*, 416-429.

806 Little, B., Anger, C. D., Ingersoll, A. P., Vasavada, A. R., Senske, D. A., Breneman, H. H.,  
807 Borucki, W. J., Galileo SSI Team (1999) Galileo images of lightning on Jupiter. *Icarus* 142,  
808 306-323.

809 Marcus, P.S. (1993). Jupiter's Great Red Spot and Other Vortices. *Ann. Rev. Astron. Astrophys.*  
810 31, 523-573.

811 Molinari, J., Duran, P., and Volaro, D. (2014). Low Richardson number in the tropical cyclone  
812 outflow layer. *Journal of the Atmospheric Sciences*. 71, 3164-3179.

813 Orton, G. S., Hansen, C., Caplinger, M., Ravine, M., Atreya, S., Ingersoll, A. P., Jensen, E.,  
814 Momary, T., Lipkman, L., Krysak, D., Zimdar, R., Bolton, S. (2017a) The first close-up  
815 images of Jupiter's polar regions: results from the Juno mission JunoCam instrument. *Geophys.*  
816 *Res. Lett.* 44, 4599-4606. doi:10.1002/2016GL072443.

817 Orton, G. S., Momary, T., Ingersoll, A. P., Adriani, A., Hansen, C. J., Janssen, M., Arballo, J.,  
818 Atreya, S. K., Bolton, S., Brown, S., Caplinger, M., Grassi, D., Li, C., Levin, S., Moriconi, M.  
819 L., Mura, A., Sindoni, G. (2017b) Multiple-wavelength sensing of Jupiter during the Juno  
820 mission's first perijove passage. *Geophys. Res. Lett.* 44, 4607-4614 doi:  
821 10.1002/2017GL073019.

822 Porco, C. C., West, R. A., McEwen, A., Del Genio, A. D., Ingersoll, A. P., Thomas, P., Squyres,  
823 S., Dones, L., Murray, C. D., Johnson, T. V., Burns, J. A., Brahic, A., Neukum, G., Veverka,  
824 J., Barbara, J. M., Denk, T., Evans, M., Ferrier, J. J., Geissler, P., Helfenstein, P., Roatsch, T.,  
825 Throop, H., Tiscareno, M., Vasavada, A. R. (2003). Cassini imaging of Jupiter's atmosphere,  
826 satellites, and rings. *Science* 299, 1541-1547.

827 Reuter, D. C., Simon-Miller, A. A., Lunsford, A., Baines, K. H., Cheng, A. F., Jennings, D. E.,  
828 Olkin, C. B., Spencer, J. R., Stern, S. A., Weaver, H. A., Young, L. A. (2007). Jupiter cloud  
829 composition, stratification, convection, and wave motion: A view from New Horizons. *Science*  
830 318, 223-225. doi 10.1126/science.1147618.

831 Rogers, J. (1995), *The Giant Planet Jupiter*, 418 pp., Cambridge Univ. Press, Cambridge, U. K.

832 Salyk, C., Ingersoll, A. P., Lorre, J., Vasavada, A., Del Genio, A. D. (2006) Interaction between  
833 eddies and mean flow in Jupiter's atmosphere: Analysis of Cassini imaging data. *Icarus* 185,  
834 430-442.

835 Sánchez-Lavega, A., Hueso, R., Eichstädt, G., Orton, G., Rogers, J., Hansen, C. J., Momary, T.,  
836 Tabataba-Vakili, F., Bolton, S. (2018). The rich dynamics of Jupiter's Great Red Spot from  
837 JunoCam – Juno images. *Astron. J.* 156, 162 (9 pp).

838 Simon-Miller, A. A., B. Conrath, P. J. Gierasch, R. F. Beebe. (2000). A detection of water ice on  
839 Jupiter with Voyager IRIS. *Icarus* 145, 454-461.

840 Simon, A. A., Li, L., Reuter, D. C. (2015a). Small-scale waves on Jupiter: A reanalysis of New  
841 Horizons, Voyager, and Galileo data. *Geophys. Res. Lett.* 42, 2612-2618, doi:  
842 10.1002/2015GL063433.

843 Simon, A. A., Wong, M. H., Orton, G. s. (2015b). First results from the Hubble OPAL program:  
844 Jupiter in 2015. *Astrophys. J.* 812:55 (8pp).

845 Simon, A. A., Hueso, R., Iñurrigarro, P., Sánchez-Lavega, A., Morales-Juberías, R., Cosentino,  
846 R., Fletcher, L. N., Wong, M. H., Hsu, A. I. de Pater, I., Orton, G. S., Colas, F., Delcroix, M.,  
847 Peach, D., Gómez-Forrellad, J.-M. (2018). A new, long-lived, jupiter mesoscale wave observed  
848 at visible wavelengths. *Astron. J.*, 156:79 (18pp).

849 Sromovsky, L. A., Baines, K. H., Fry, P. M., Carlson, R. W. (2017) A possibly universal red  
850 chromophore for modeling color variations on Jupiter. *Icarus* 291, 232-244. doi  
851 10.1016/j.icarus.21016.12.014.

852 Sugiyama, K., Nakajima, K., Odaka, M., Kuramoto, K., Hayashi, Y.-Y. (2014). Numerical  
853 simulations of Jupiter's moist convection layer: Structure and dynamics in statistically steady  
854 states. *Icarus* 229, 71-91.

855 Sugiyama, K., Nakajima, K., Odaka, M., Kuramoto, K., Hayashi, Y.-Y. (2014). Corrigendum to:  
856 "Numerical simulations of Jupiter's moist convection layer: Structure and dynamics in  
857 statistically steady states. *Icarus* 229, 71-91". *Icarus* 231, 407-408.

858 Tabataba-Vakili, F., Rogers, J. H., Eichstädt, G., Orton, G. S., Hansen, C. J., Momary, T. W.,  
859 Sinclair, J. A., Giles, R. S., Caplinger, . A., Ravine, M. A., Bolton, S. J. (2019). Long-term  
860 tracking of circumpolar cyclones on Jupiter from polar observations with JunoCam. *Icarus*. In  
861 press.

862 Trier, S.B., Sharman, R.D., Fovell, R.G., Frehlich, R.G. (2010). Numerical simulation of radial  
863 cloud bands within the upper-level outflow of an observed mesoscale convective system.  
864 *Journal of the Atmospheric Sciences*. 67, 2990-2990.

865 West, R.A., Strobel, D. F., Tomasko, M. G. (1986). Clouds, aerosols, and photochemistry in the  
866 Jovian atmosphere. *Icarus* 65, 161-217. doi 10.1016/0019-1035(86)90135-1

867 Wong, M. H., Simon, A. A., Tollefson, J. W., de pater, I., Barnett M., Hsu, A. I. Stephens, A.,  
868 Orton, S. G. Fleming, S. W., Januszewski, W., Roman, A., Goullaud, C., Bjoraker, G. L,  
869 Atreya, S. K., Adriani, A. (2020). High-resolution UV/optical/IR imaging of Jupiter in 2016–  
870 2019. *Astrophysical Journal Supplement Series*. Submitted.

871 Yang, Q. and Geerts, B. (2014). Horizontal convective rolls in cold air over water:  
872 Characteristics of coherent plumes detected by an airborne radar. *Monthly Weather Rev.* 134,  
873 2373-2395.

874 Young, R. M. B., Read, P. L. (2017). Forward and inverse kinetic energy cascades in Jupiter’s  
875 turbulent weather layer. *Nature Physics* 13, 1135.

876

877

878 Tables  
879

Observing Platform (year)	Associated Publications	Range of Planetocentric Latitudes	Range of Wavelengths (km)
Voyager (1979)	Hunt & Muller (1979), Flasar & Gierasch (1986)	27° S-27° N	70-430
Galileo (1996)	Bosak & Ingersoll (2002)	13° S	300
Galileo (1999)	Arregi et al. (2009), Simon et al. (2015)	0.2° N, 3.6° N	155-205
Galileo (2001)	Arregi et al. (2009)	1.8° S	195-215
New Horizons (2007)	Reuter et al. (2007), Simon et al. (2015)	0° -1.1° N	280-330
Juno/JIRAM (2017)	Adriani et al. (2018), Fletcher et al. (2018)	14° -15° N	1400-1900
Juno/JunoCam (2017)	Sánchez-Lavega et al. (2018)	16° S	35
Hubble Space Telescope (2012-2018)	Simon et al. (2018)	14.5° ±2.5° N	1220-1340
Ground-Based Visible Observations (2017)	Simon et al. (2018)	14.5° ±2.5° N	1220-1340
Ground-Based 5-μm Observations (2016-2017)	Fletcher et al. (2018)	14.5° ±2.5° N	1300-1600

880  
881 *Table 1. Summary of previous observations of small-scale waves in Jupiter’s clouds detected at*  
882 *5 μm or shorter wavelengths. (Some values are also displayed in Figure 16.) The waves*  
883 *addressed by Sánchez-Lavega et al. (2018) are associated with the Great Red Spot.*  
884

885  
886  
887  
888  
889  
890  
891  
892  
893  
894

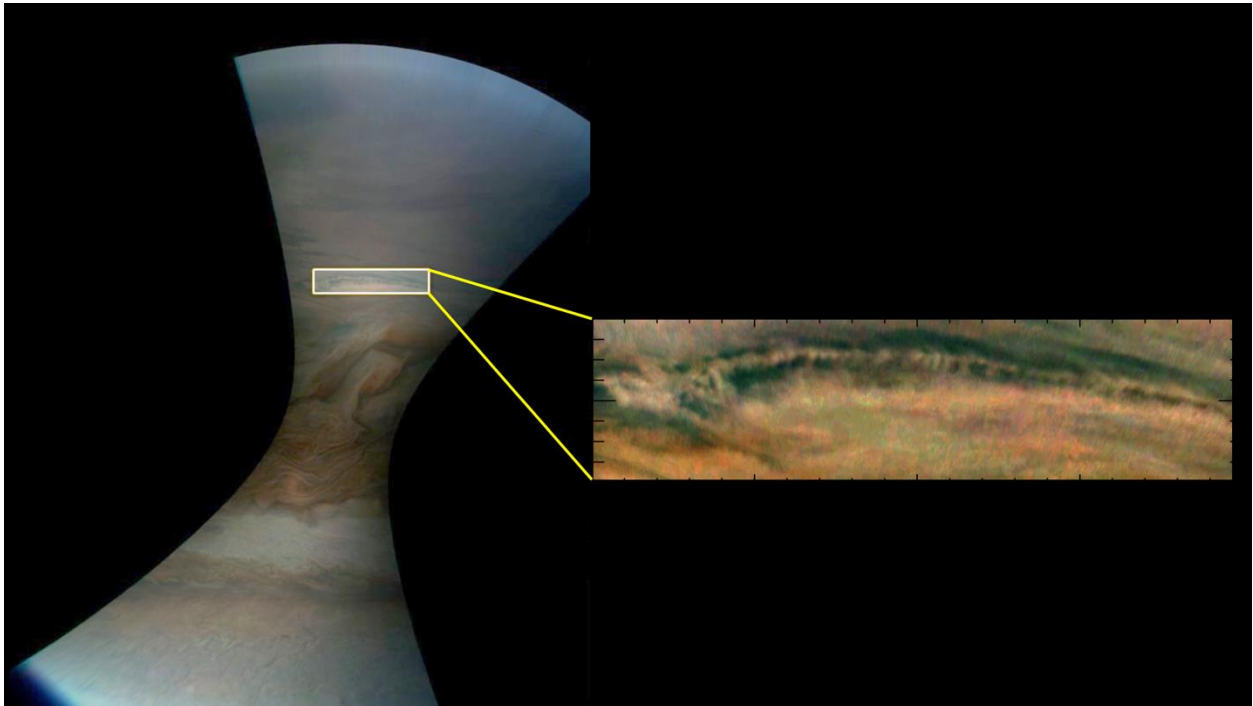
Type of Wave-Like Feature (section where discussed)	Number of Features
Long packets, short crests (3.2.1)	100
Wide wave crests (3.2.2)	25
Curved packets (3.2.1)	9
Small white clouds (3.2.3)	9
Regularly spaced dark features (3.2.7)	6
Emanating from vortex (3.2.5)	4
Extremely long curved features (3.2.2)	2
Lee waves (3.2.4)	1

895  
896  
897  
898  
899  
900  
901  
902  
903

*Table 2. Number of features in each morphological category, listed in order of frequency. These include features not illustrated in the figures associated with the main article but included in the Supplementary Information file. The total number of waves or wave-like features is 157. The category of waves with long packets and short crests dominates the total. Quantitative properties of these waves are shown in the Table of Section SI2 of the Supplemental Information file. They are also shown graphically in Figs. 16, 17 and Figs. SI3-1 through SI3-3 of the Supplemental Information file.*

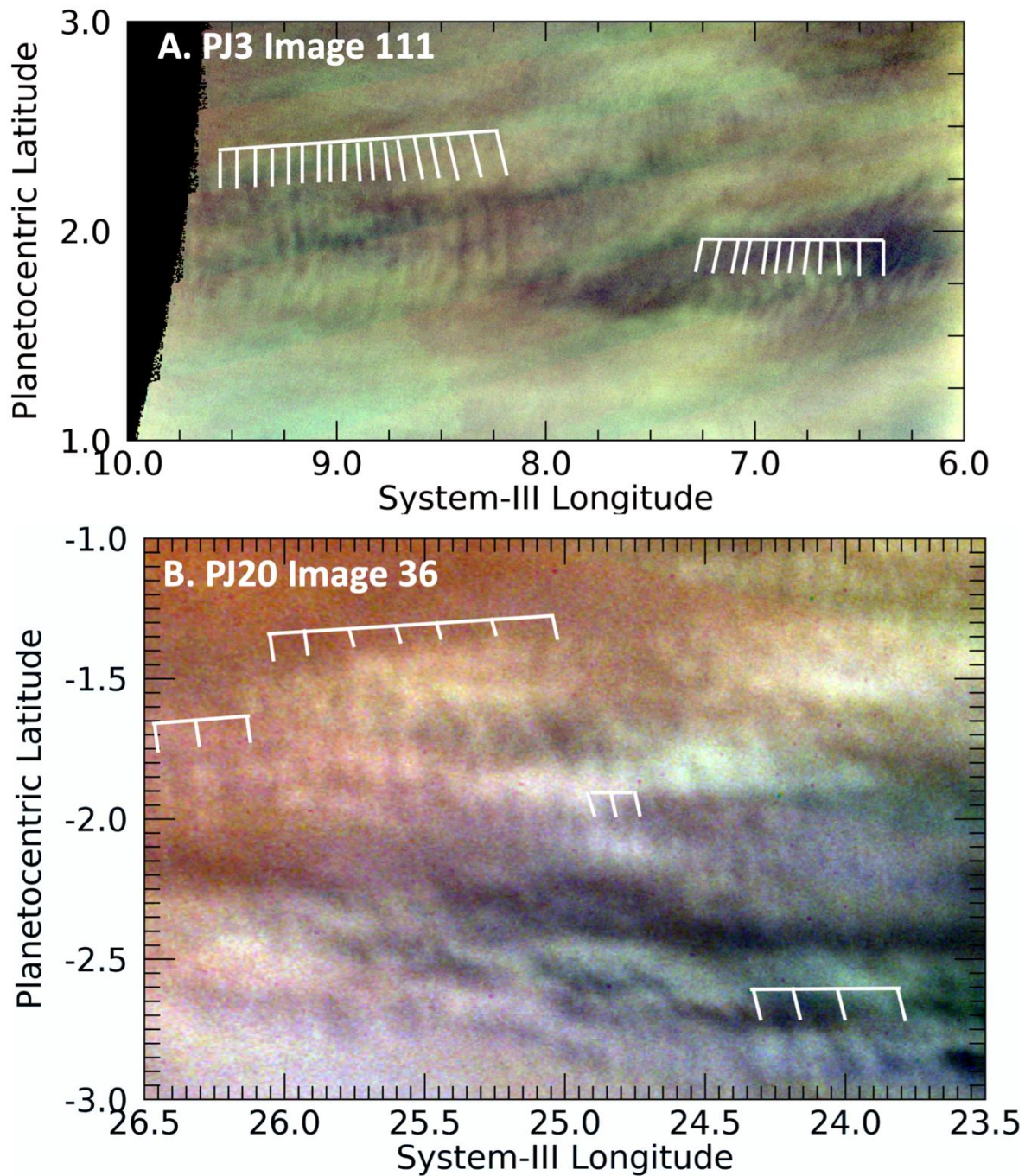
904  
905

## Figures



906  
907  
908  
909  
910  
911  
912  
913

*Figure 1. Example of excerpting a portion of a wave-like feature from a JunoCam image from planetocentric latitudes 3°S - 4°S. This is a cylindrical mapping of a color-composited Image JNCE\_2017297\_09C00088\_V01 (which here and elsewhere we simply identify as Image 99 from PJ9. The extracted panel is also shown as Figure 10B and in the Supplemental Information file as Figure PJ09\_88 with a grid indicating the location of peak radiances in the wave-like feature.*



915

916

917 *Figure 2. Excerpts from JunoCam color-composite maps of images in PJ3 illustrating isolated*918 *wave packets with shorter wave fronts that are orthogonal to the orientation of the wave packet.*919 *In this and all other similar figures in this report, the colors have been stretched extensively in*920 *order to make the waves as visible as possible; they have absolutely no relationship with the true*921 *colors of the planet. In this and some sequent images here and in the Supplemental Information*922 *file, broad vertical or diagonal colored bands are artefacts of strong image enhancement to*923 *distinguish otherwise faint features.*

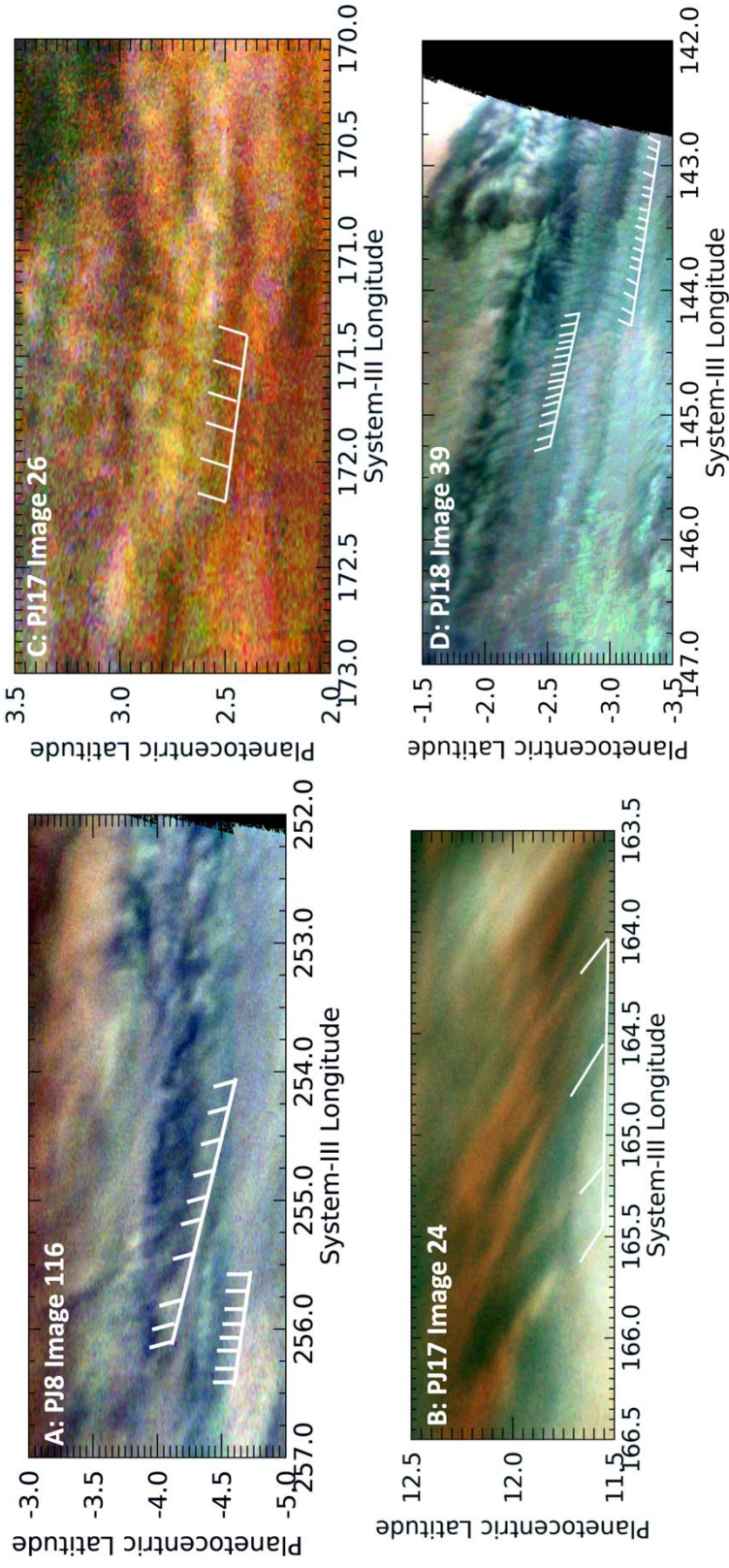


Figure 3. Excerpts from JunoCam maps of images in PJ8 (Panel A), PJ17 (Panels B and C) and PJ18 (Panel D). These illustrate individual wave packets with shorter wave fronts that are not-orthogonal (i.e. they are “tilted”) with respect to the orientation of the wave packet direction.

928  
929  
930  
931

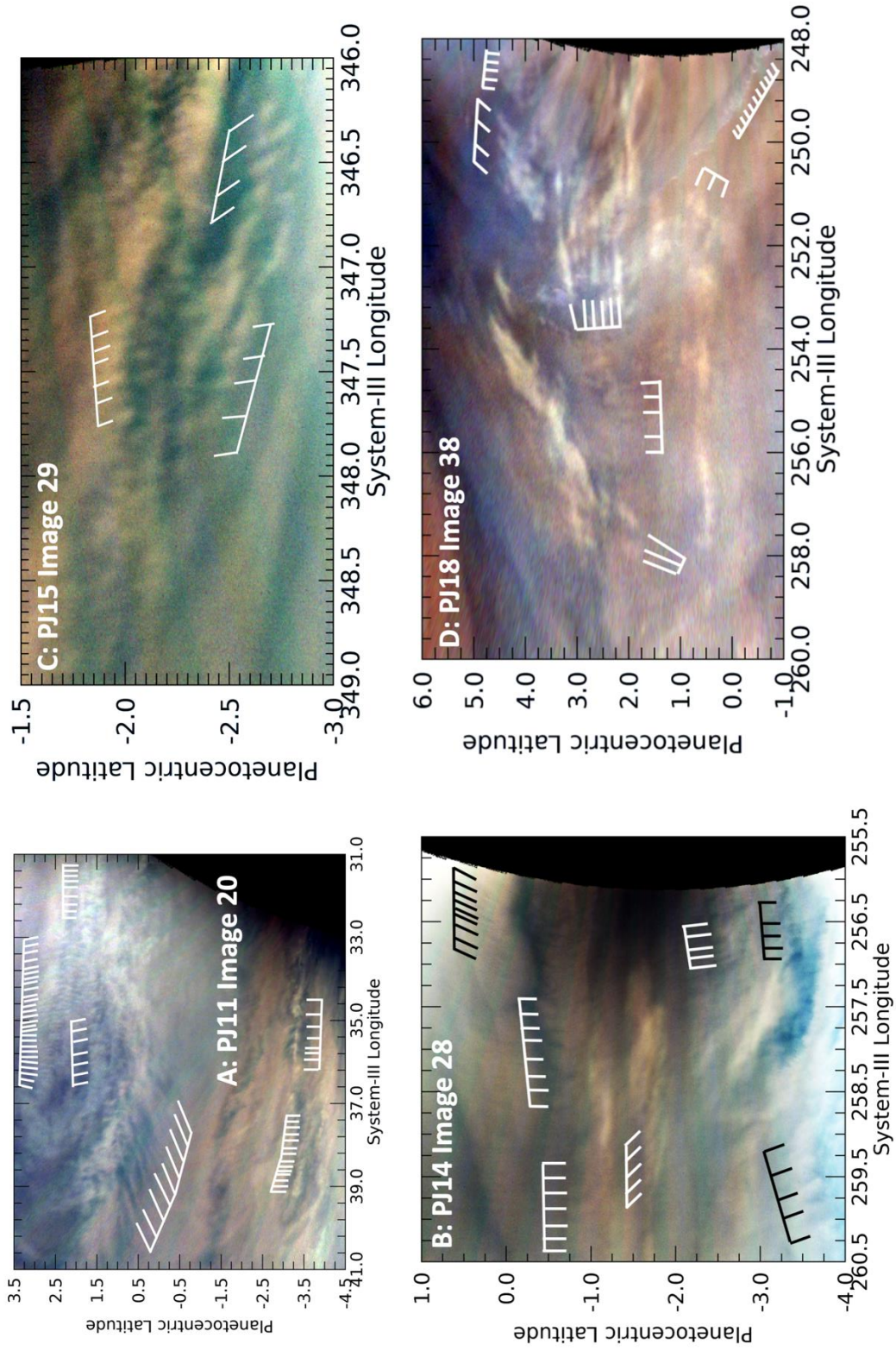


Figure 4. A variety of wave morphologies detected near the equator. As shown in these images, the Equatorial Region is often populated with both short and long wave trains with both orthogonal and "tilted" wave fronts, often overlapping. Toward the bottom of Panels A and D are a set of waves defined by discrete white clouds, more of which are shown closer up in Figure 8.

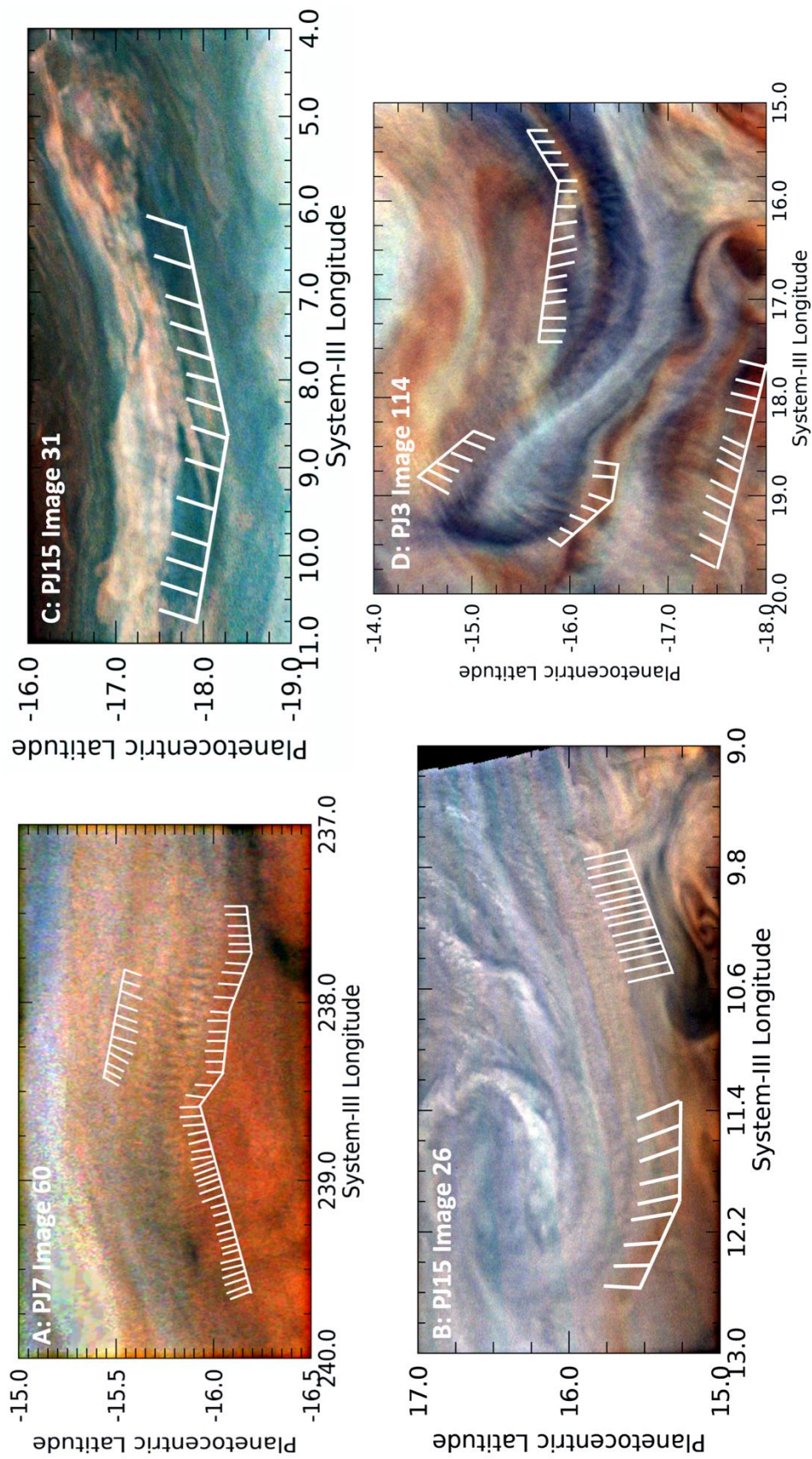
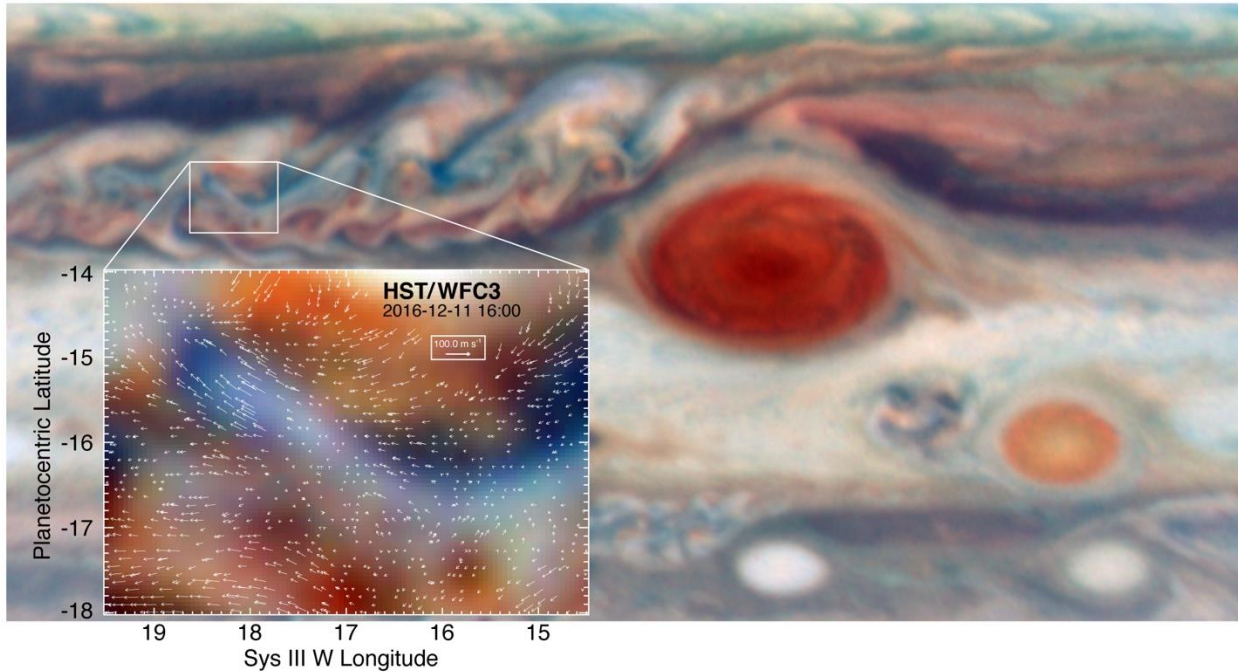
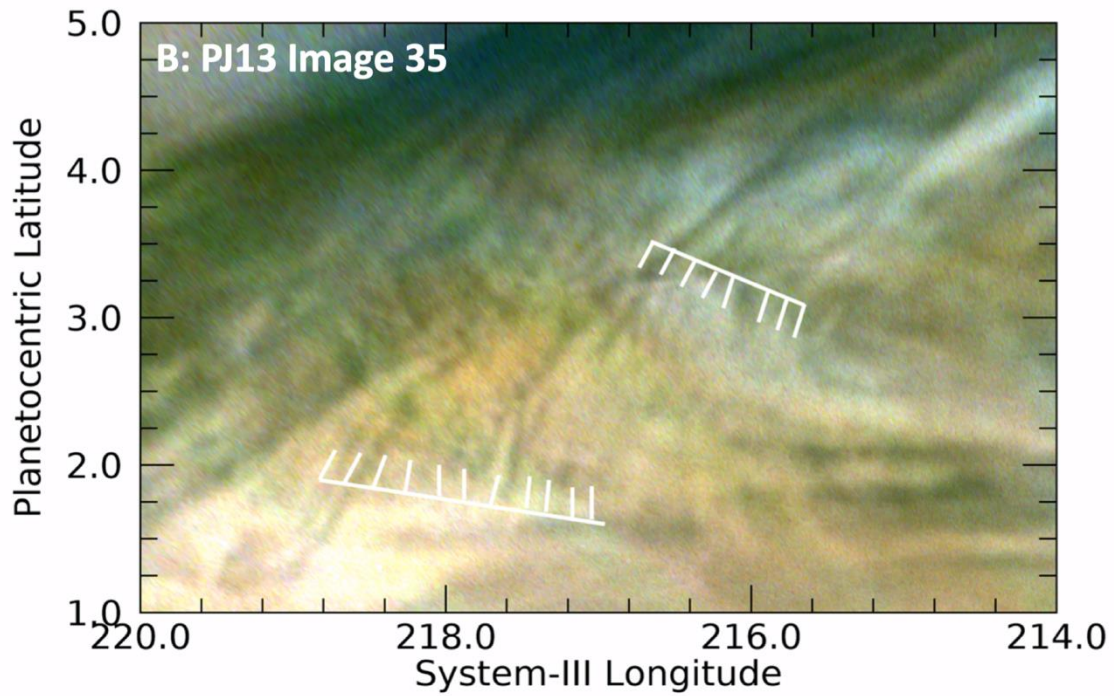
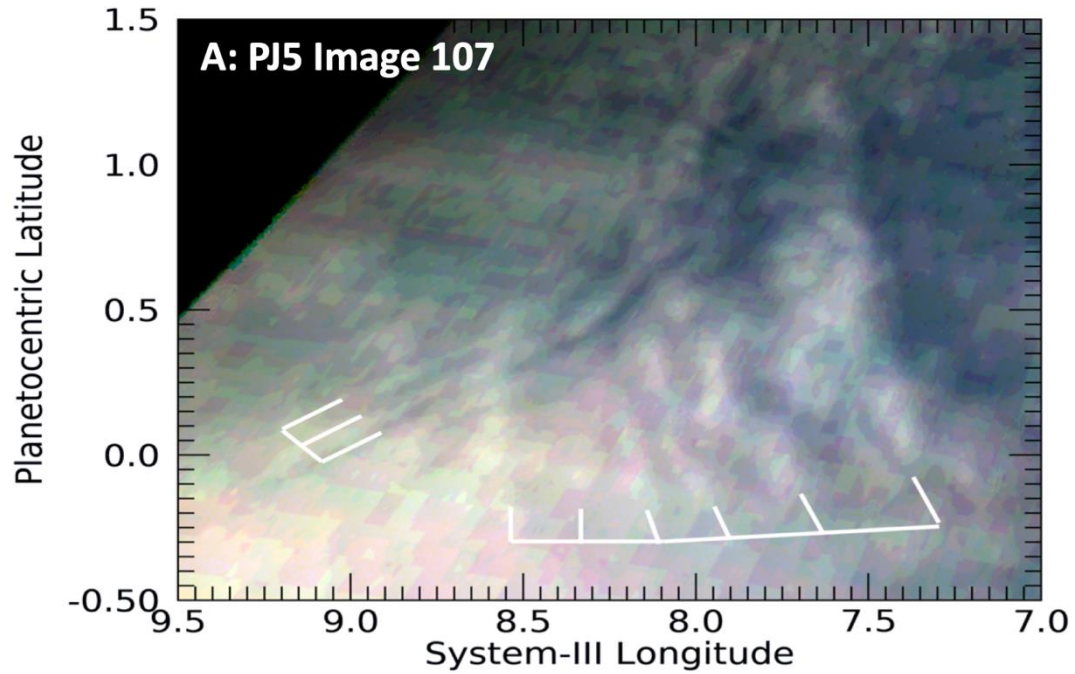


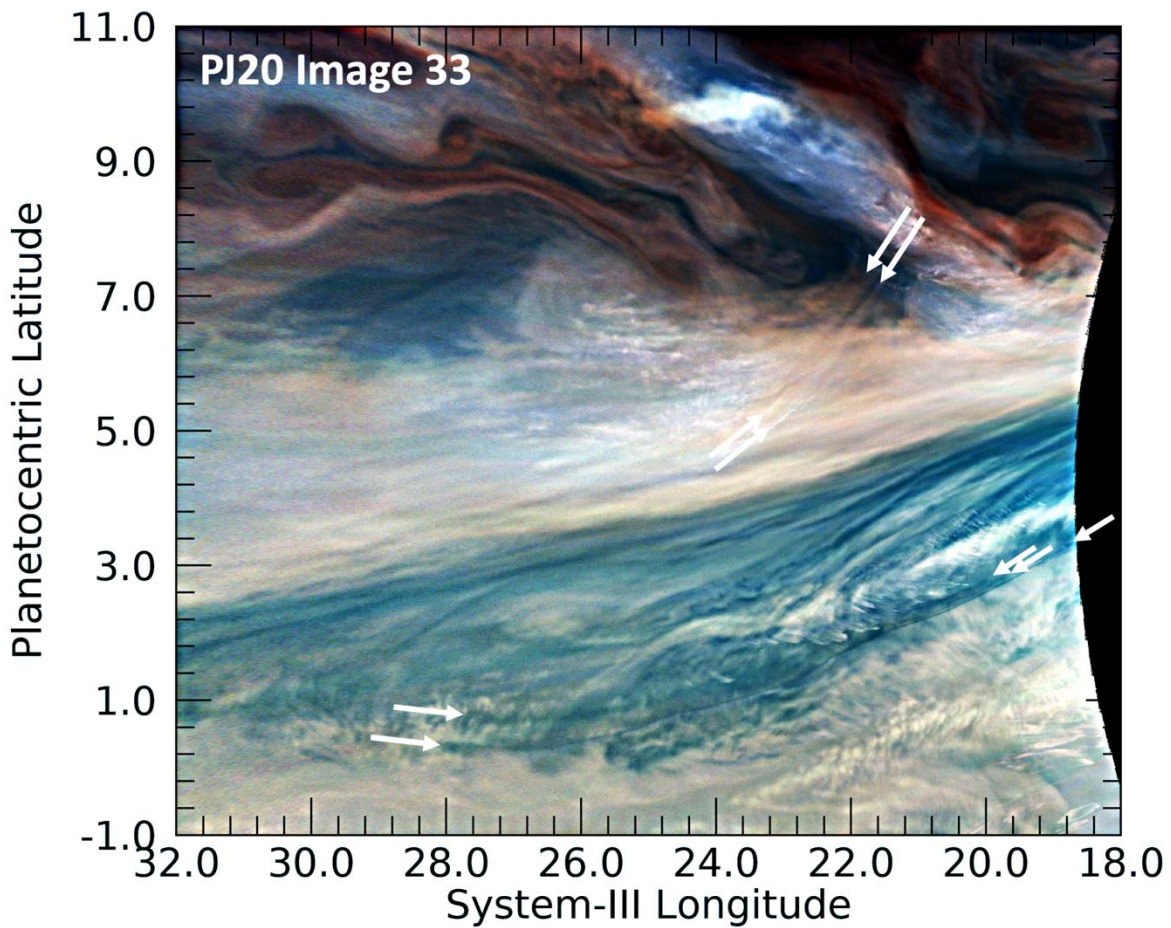
Figure 5. Examples of short wavefronts associated with a curved wave packet. *A:* Wavefronts associated with the curvature of the northern boundary of the GRS. A version of this panel appears in Figure 8 of Sánchez-Lavega et al. (2018). *B:* Wavefronts along the southern edge of an anticyclonic eddy in the NEB. *C:* Wavefronts on the south edge of a cyclonic circulation in the SEB. *D:* Wavefronts that cross a relatively dark lobate feature in the South Equatorial Belt (SEB), a part of a turbulent region west of the Great Red Spot.



933  
 934 *Figure 6. Contextual HST WFC3 image for Figure 5D, showing its position with respect to the*  
 935 *GRS. The inset shows the wind field derived from tracking cloud features over a 45-minute*  
 936 *interval, as a residual after subtracting the mean zonal wind profile. The winds appear to be a*  
 937 *maximum at the western (left) end of the blue lobate feature, with a marked drop in velocities,*  
 938 *i.e. a region of wind shear, at the edges of the feature. This image was taken within a few*  
 939 *minutes of the time at which the JunoCam image in Fig. 5D was observed*  
 940



941  
 942 *Figure 7. Excerpts from maps showing waves whose wave fronts are larger than the wave packet*  
 943 *length. Both are curved and located in the Equatorial Zone. Panel A shows a pair of wave*  
 944 *packets, overlapping each other, the westernmost of which contains at least three wave fronts*  
 945 *that are much longer than the packet. The overlapping easternmost wave packet has wave fronts*  
 946 *and a length that are roughly equal in size. Panel B shows a series of curved waves that appear*  
 947 *to extend past the boundaries of the full image*



948  
 949 *Figure 8. Extremely long, curved features detected in PJ20. Two unusually long features that*  
 950 *may be waves were detected near the southwestern extension (“festoon”) of a 5- $\mu$ m hot spot,*  
 951 *seen here as the dark area. North of the dark area of the festoon is a pair of lines, whose*  
 952 *beginnings and ends are marked by white arrows. Among the many waves found south of the*  
 953 *festoon, is a set of three closely spaced parallel lines, noted by the arrows that do not begin or*  
 954 *end at the same position. Only for two of them is the western end evident. We note that some mild*  
 955 *unsharp masking has been applied to this image in order to resolve for the reader the three dark*  
 956 *curves at their eastern ends. (The locations of many more of the waves present in this figure are*  
 957 *indicated in Figure PJ20\_34 in the Supplemental Information file.)*

958  
 959  
 960  
 961

962  
 963  
 964  
 965  
 966

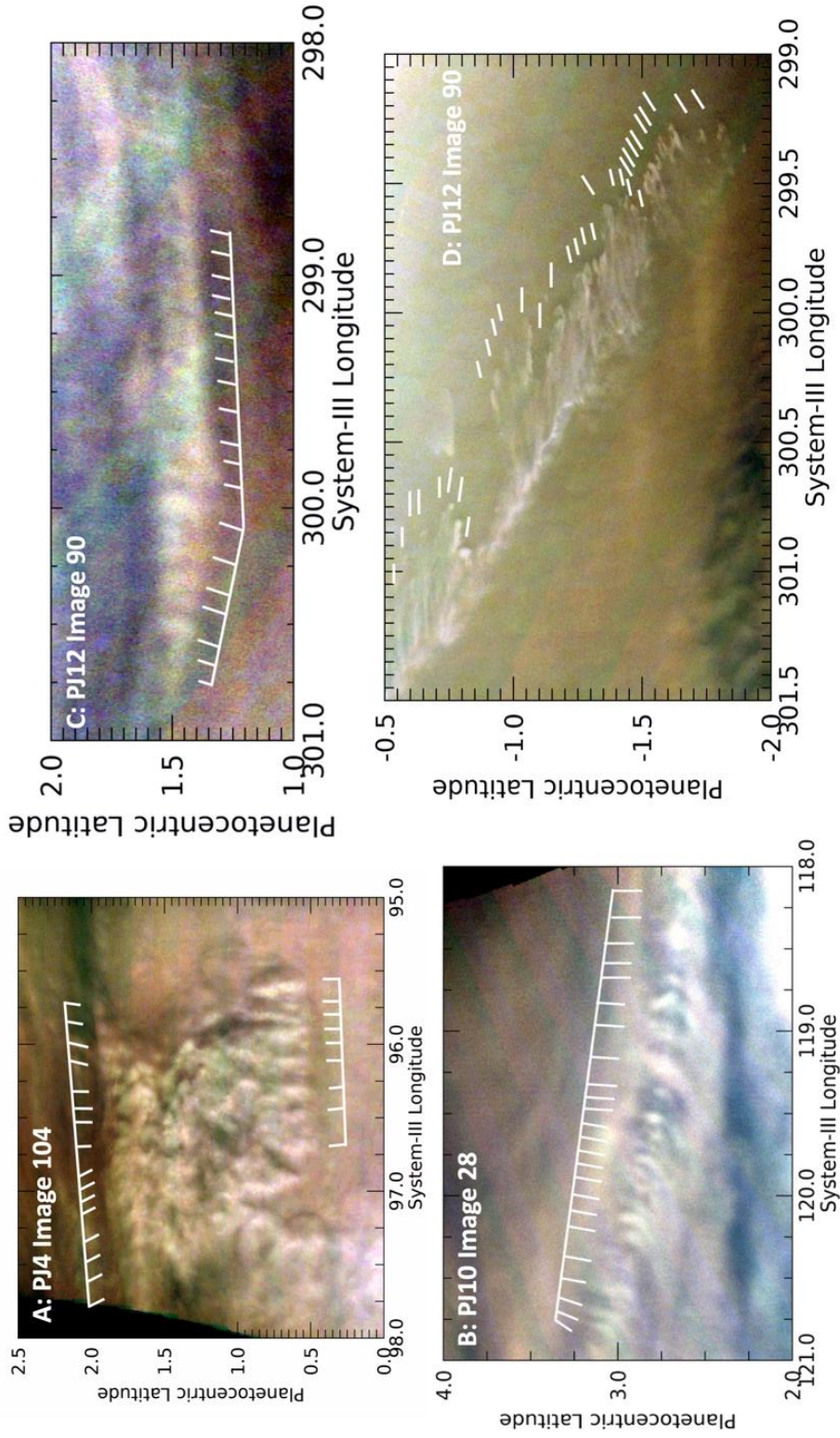
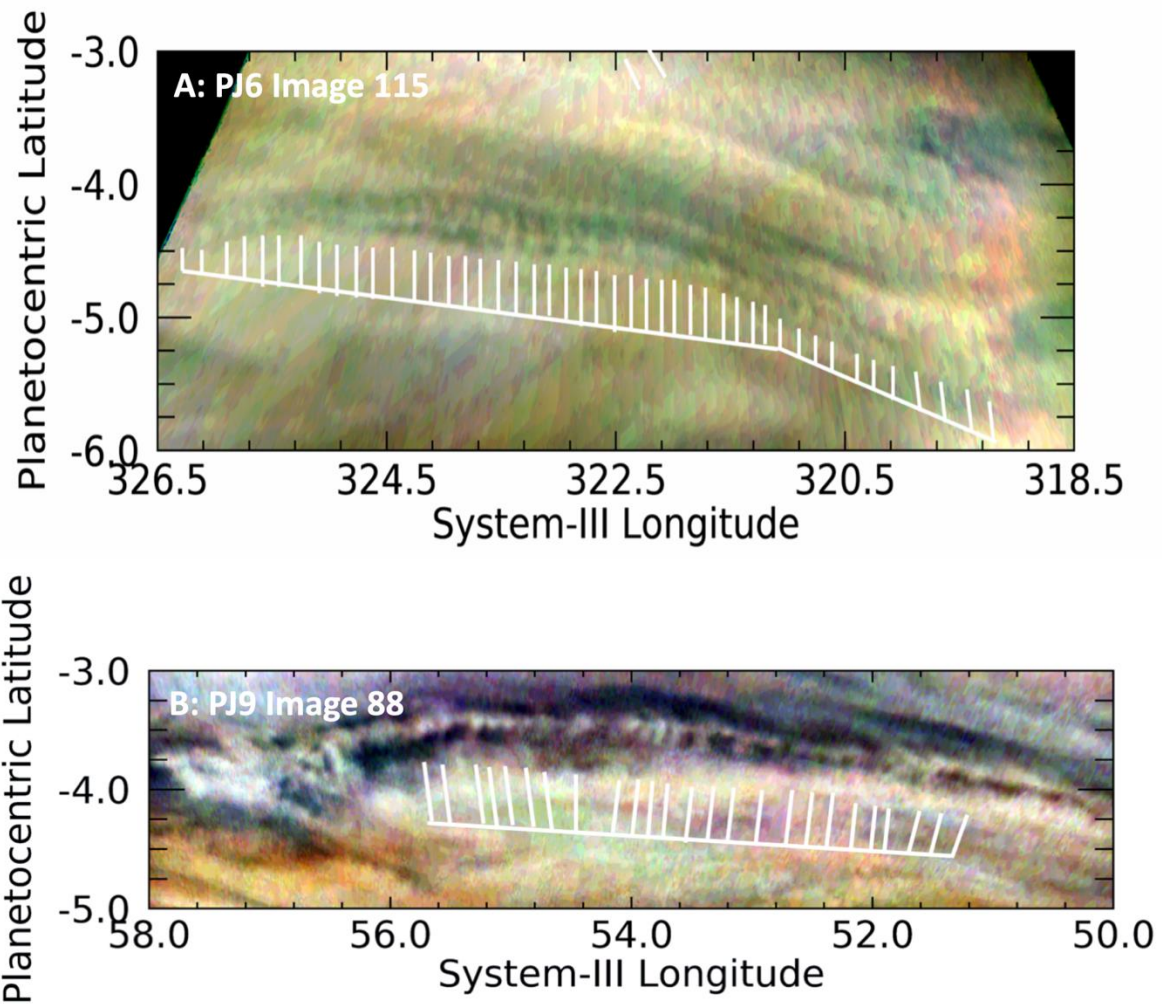


Figure 9. Examples of wave packets defined by bright clouds, all in the Equatorial Zone. Panel A shows a wave packet whose length is roughly equal to its width. Its constituent clouds are clearly higher than their surroundings, given the strong topographic clues from consistent shadowing on their eastern sides. Panel B shows a line of regular clouds with longer, curved southwestern extensions. Panel C shows a similar wave packet of white clouds with narrow wavefronts and a slight curvature. Panel D shows a very curious type of irregular wave-like feature, extracted from the northeastern portion of Fig. PJ12\_90a in the Supplemental Information file. The feature is reminiscent of ocean foam, with side-by-side elongated features that are not uniformly directed and may be higher than the surrounding cloud deck, with a consistent darkening on their eastern sides that might be shadowing.



967  
 968 *Figure 10. Two detections of regular patterns of relatively bright clouds apparently associated*  
 969 *with a fainter central bright region. Both instances involve curved lines. The wave packet in*  
 970 *Panel A is associated with a similar but fainter pattern to its north, whereas the wave packet in*  
 971 *Panel B has no such association. Both are in the southern component of the Equatorial Zone.*  
 972

973  
974  
975

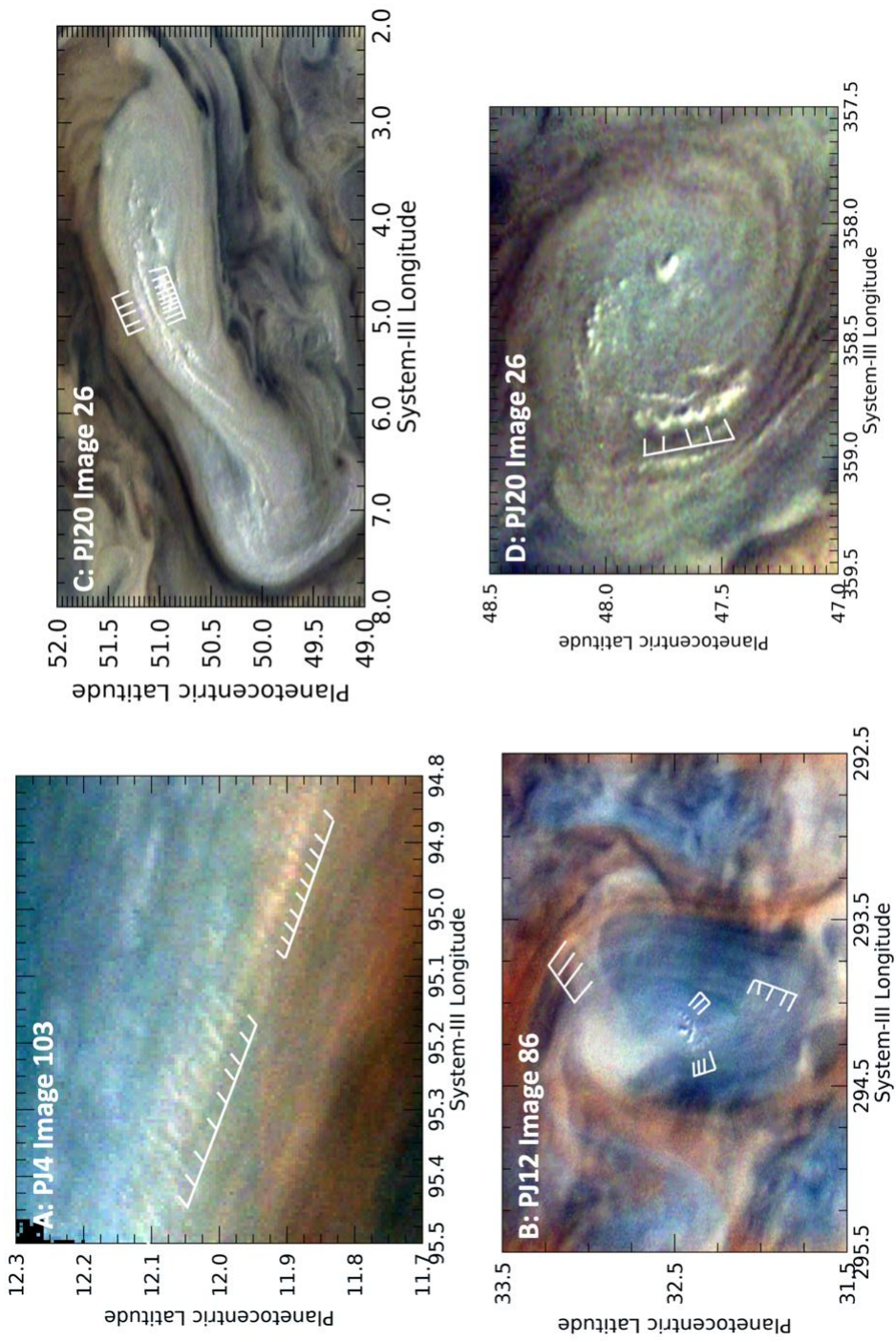
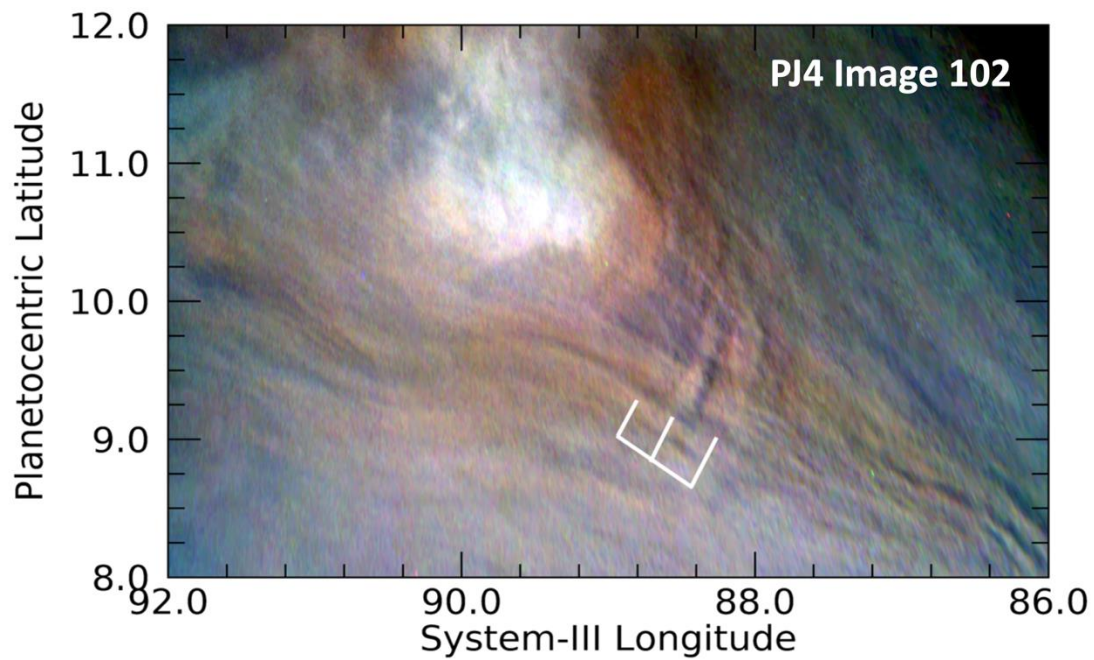
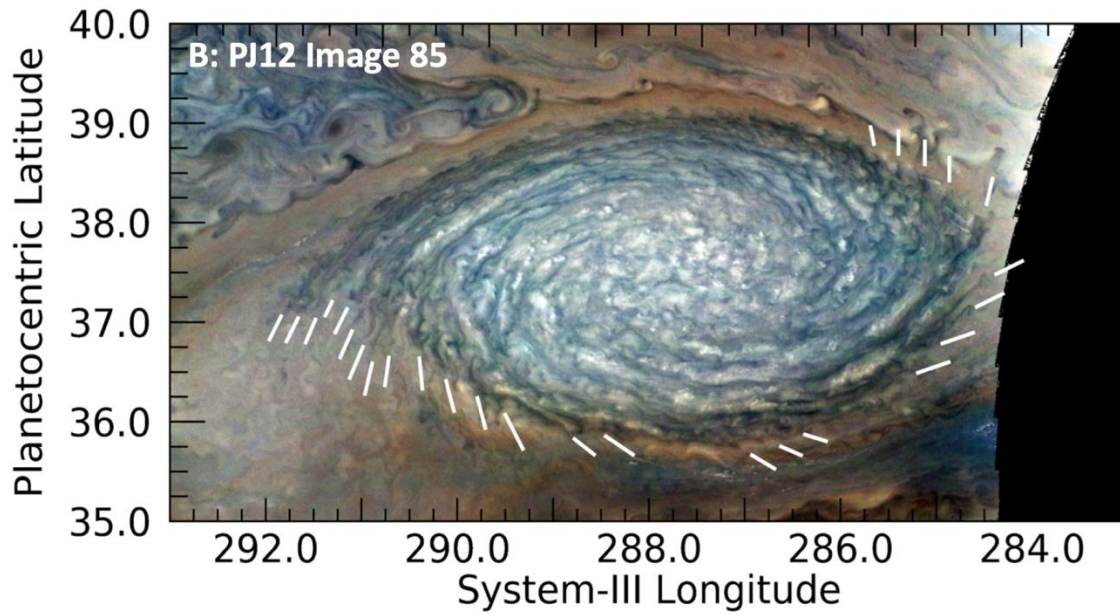
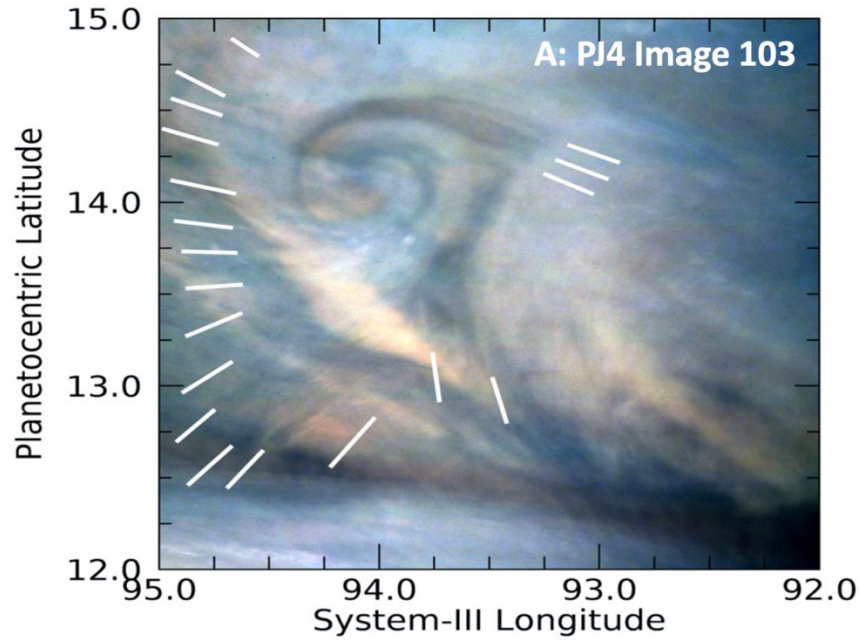


Figure 11. Distinct, very small-scale white clouds with regular spacing. The spacing and the distinct arrangement along a discrete path suggest a wave-like structure. Panel A shows an expanded portion of Fig. PJ04\_103b in the Supplemental Information file. Panel B shows a bright cloud, accompanied by short linear arrays of similar bright clouds in an anticyclonic feature in the North North Temperate Belt (NNTB). Panels C and D both show features from the same image in an area just south of the prograde jet at 53°N. From their morphologies, they are both most likely to be anticyclonic vortices.

976



977  
978 *Figure 12. The single unambiguous detection of lee waves in the JunoCam images. We can*  
979 *presume that the long streaks appearing diagonally in this figure are tracking the streamlines of*  
980 *local winds. The lee waves indicated by the white grid lines are orthogonal to the elongated*  
981 *streaks and are likely to be downwind of the bright convective plume in the upper part of this*  
982 *image.*  
983



984  
 985  
 986  
 987  
 988  
 989  
 990

*Figure 13. Wave-like features detected near vortices. Panel A shows a very compact cyclonic feature with a set of extended radial wavefronts in the North Equatorial Belt (NEB). Panel B shows a regular set of dark lines emerging from the ends of the internal spiral structures in an anticyclonic white oval.*

994  
993  
992  
991

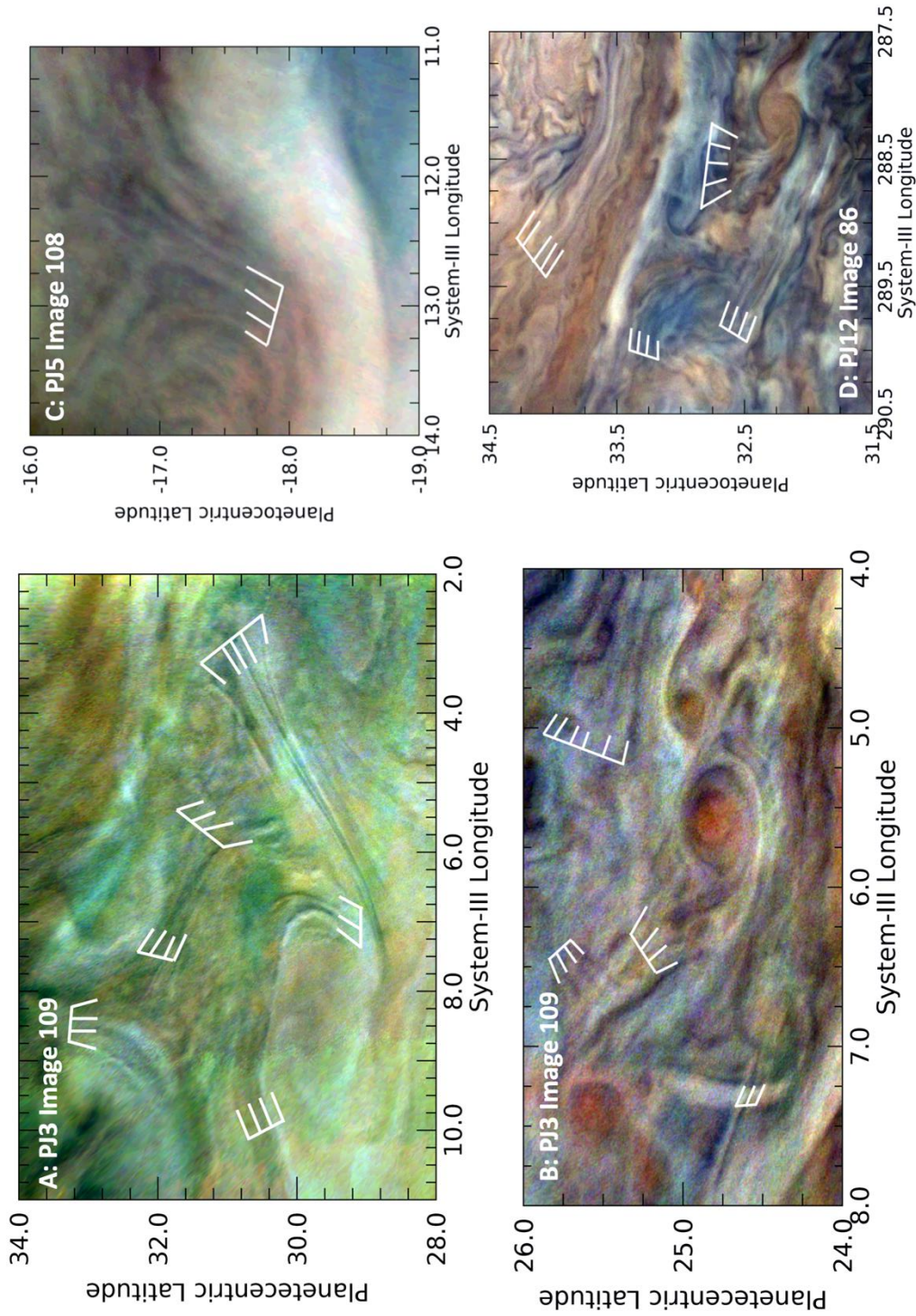
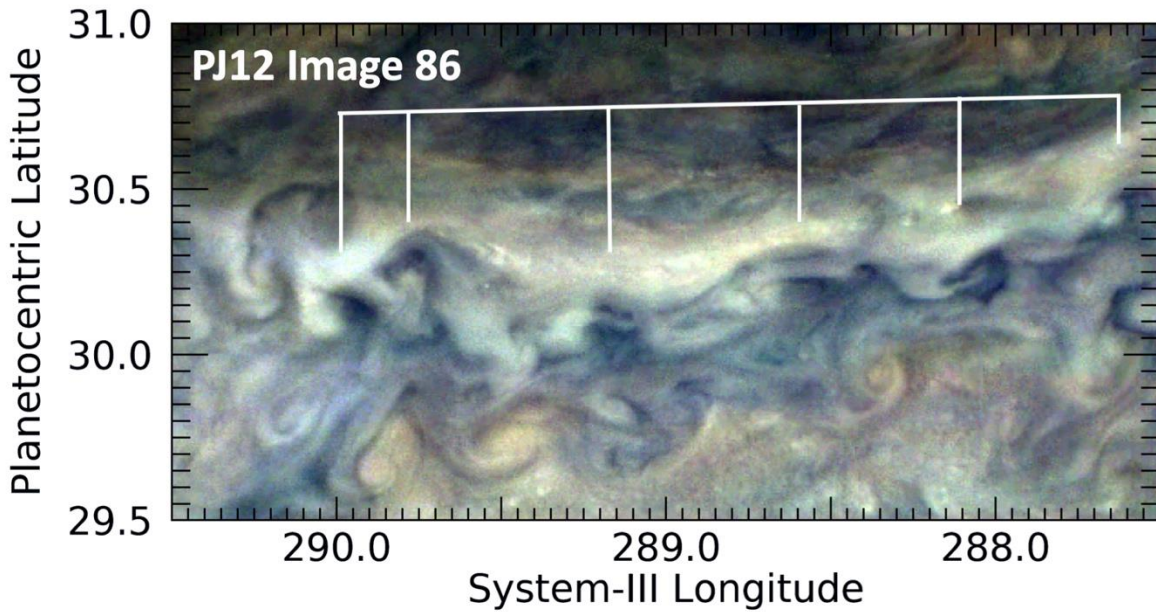
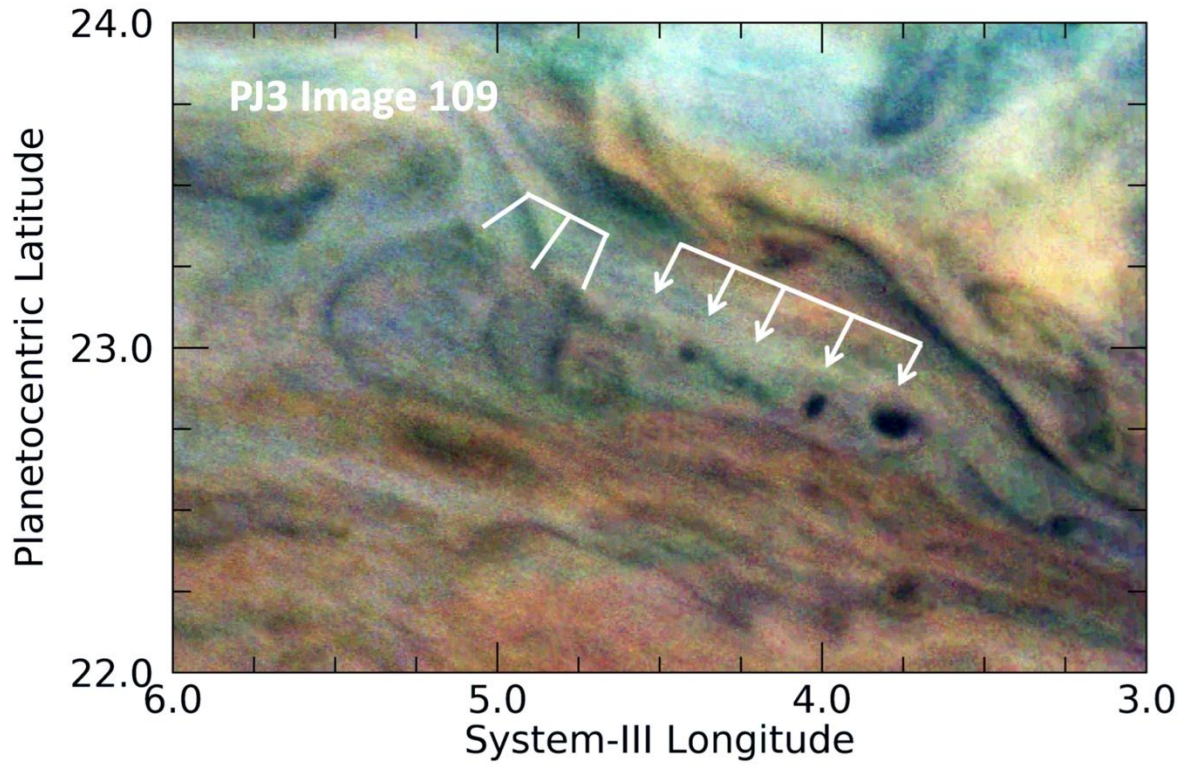


Figure 14. Examples of very long and nearly evenly spaced parallel streaks. Panel A shows several of these detected in a limited region of the North Temperate Zone (NTZ). Panel B shows a region just south of the area in Panel A on the same perijove in the northern component of the North Temperate Belt (NTBn). Panel C shows parallel streaks located in a pale strip of the southern component of the South Equatorial Belt (SEBs). Panel D shows multiple examples of parallel cloud streaks in the North North Temperate Belt (NNTB).



996

997

998

999

1000

1001

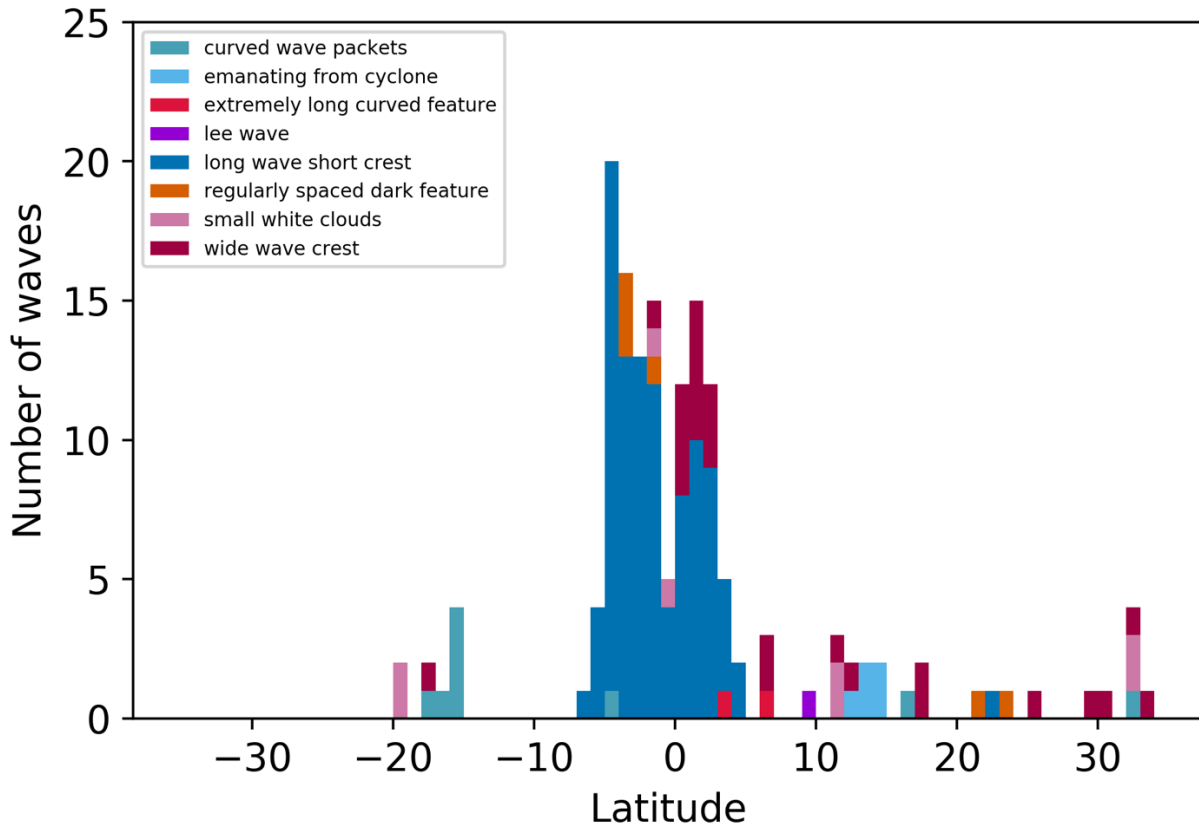
1002

1003

1004

Figure 15. Unusual quasi-wave-like features in the northern hemisphere. Panel A illustrates three curved wavefronts next to relatively dark circular features indicated by the arrows. Panel B shows a series of repeated patterns in the North Temperate Zone.

1005



1006

1007

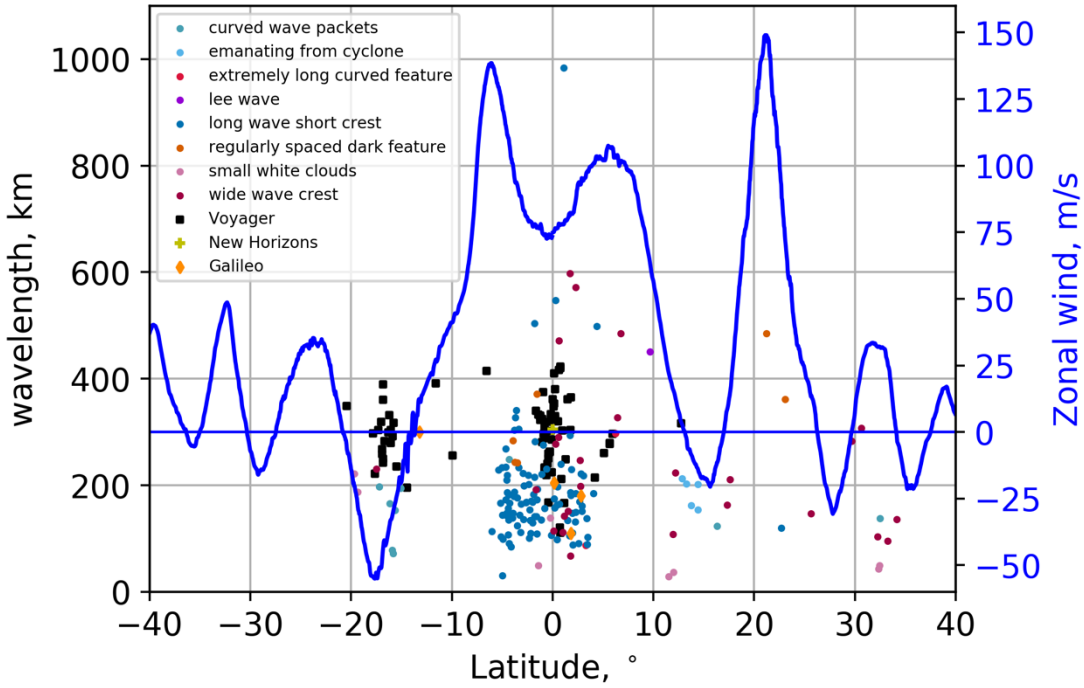
1008

1009

1010

1011

*Figure 16. Histogram of waves and wave-like features detected in PJI-20 by JunoCam. Different types of waves and wave-like features are denoted by different colors and identified by the key. Each corresponds to a different wave morphology as discussed in Section 3.2. The bin size is 1° in latitude.*



1012  
 1013 *Figure 17. Wavelengths of waves and wave-like features detected in PJ1, PJ3-PJ20 by JunoCam.*  
 1014 *Measurements of different types of wave morphologies are color-coded as in Figure 15. Mean*  
 1015 *zonal wind velocities for 2017-2018 (Wong et al. 2020) are plotted in blue. Values for Voyager,*  
 1016 *New Horizons and Galileo are taken from their respective references in Table 1. Wavelengths*  
 1017 *for wave packets detected by HST and ground-based images (Simon et al. 2018, Fletcher et al.*  
 1018 *2018) are greater than 1100 m/s and clustered around 14.5°N (see Table 1).*  
 1019  
 1020  
 1021